

On the Selective Oxidation of a 0.15C-6Mn-2Al-1Si Third-Generation Advanced High Strength Steel During Two-Stage Annealing Treatments



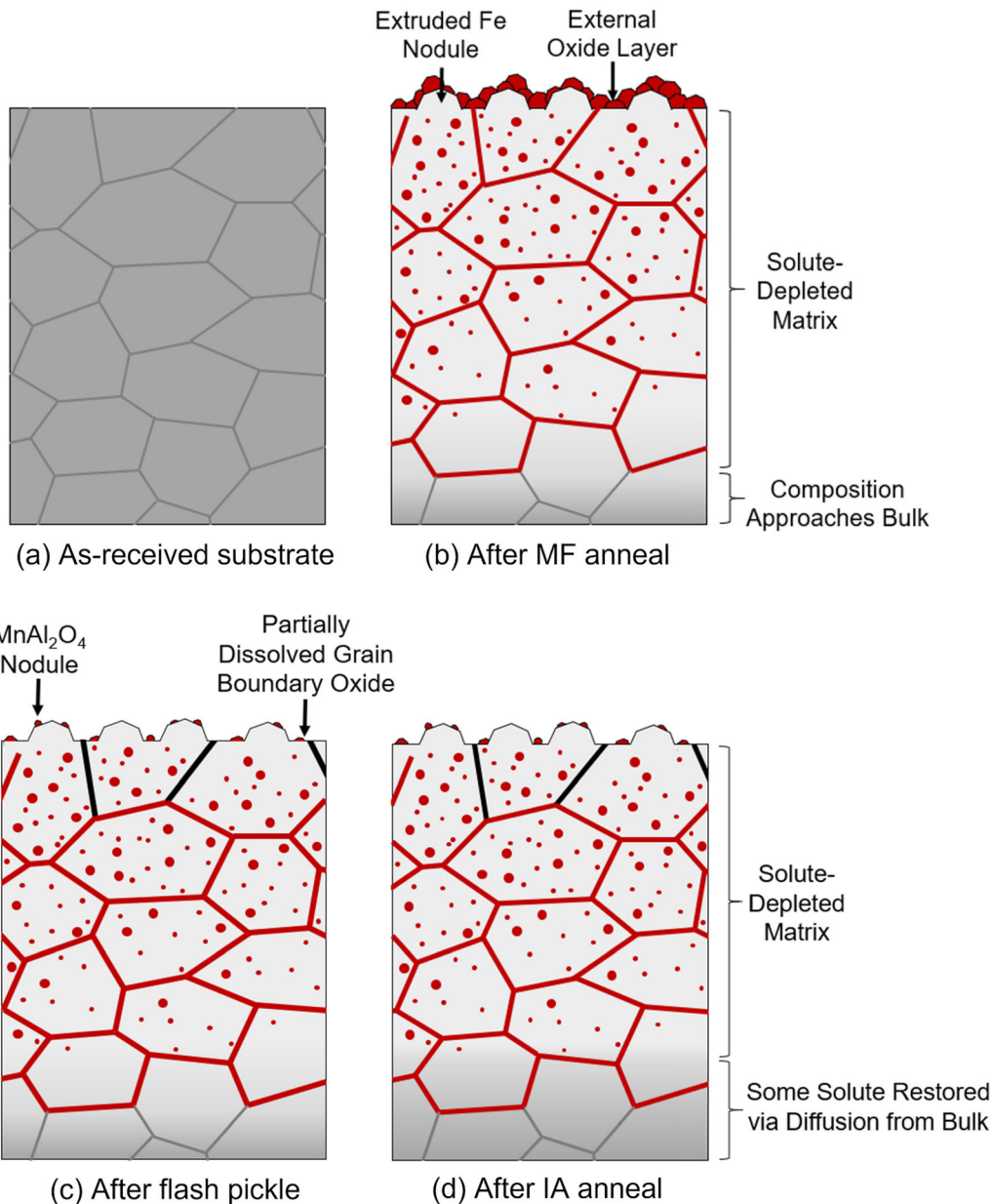
DANIELLA M. PALLISCO and JOSEPH R. MCDERMID

The selective oxidation of a 0.15C-5.6Mn-1.9Al-1.1Si (wt pct) prototype third-generation advanced high-strength steel during dew point-controlled two-stage annealing with intermediate flash pickling was documented. After austenitization annealing at 1163 K for 600 s, the surfaces had compact nodules of MnO on top of co-precipitated nodules of $\text{MnSiO}_3/\text{Mn}_2\text{SiO}_4$ and MnAl_2O_4 . The intermediate flash pickling treatment dissolved the external MnO and Mn-Si oxides, leaving behind small, widely spaced MnAl_2O_4 nodules with significant fractions of metallic Fe exposed. Subsequent intercritical annealing at 983 K for 120 s resulted in no significant changes to the MnAl_2O_4 nodules due to solute depletion from the near-surface matrix during austenitization annealing. The resulting surfaces were relatively barren of external oxides and had significant fractions of metallic Fe boldly exposed, which are promising for reactive wetting by conventional continuous galvanizing baths.

DANIELLA M. PALLISCO and JOSEPH R. MCDERMID are with the Centre for Automotive Materials and Corrosion, Department of Materials Science and Engineering, McMaster University, Hamilton, ON, L8S 4L8, Canada. Contact e-mail: mcdermid@mcmaster.ca

Manuscript submitted August 23, 2022; accepted January 7, 2023.

Article published online February 20, 2023



<https://doi.org/10.1007/s11661-023-06985-2>

© The Minerals, Metals & Materials Society and ASM International 2023

I. INTRODUCTION

THE development of advanced high-strength steels (AHSS) has been motivated by increasing demands on the automotive industry to improve fuel efficiency while improving passenger safety. In particular, third-generation (3G) AHSS are under investigation due to their superior mechanical properties relative to the currently employed first generation AHSSs while being leaner in composition than second generation AHSSs.^[1-4] Among the proposed strategies for 3G AHSS development,

medium-Mn 3G AHSS grades are promising candidates for automotive body-in-white applications due to their compatibility with continuous galvanizing line (CGL) processing capabilities.^[5-10] This is highly desirable since the CGL is a cost-effective means of providing the substrate with robust corrosion protection.

The selective oxidation of primary alloying elements (specifically Mn, Si, and Al) in the CGL annealing furnace is a well-documented phenomenon.^[11-17] For example, it is known that the furnace process atmosphere oxygen partial pressures (pO_2) employed in the

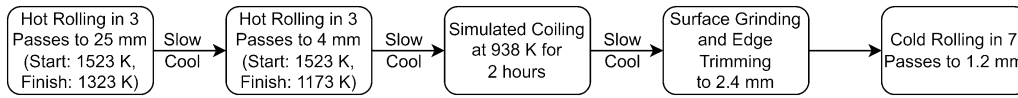


Fig. 1—Thermomechanical processing route of the experimental steel.

Table I. Chemical Composition of the Experimental Substrate (in Wt Pct and At. Pct)

	C	Mn	Al	Si	Mo	Ti	Fe
Wt Pct	0.15	5.56	1.89	1.10	0.08	0.01	balance
At. Pct	0.67	5.45	3.77	2.11	0.05	0.01	balance

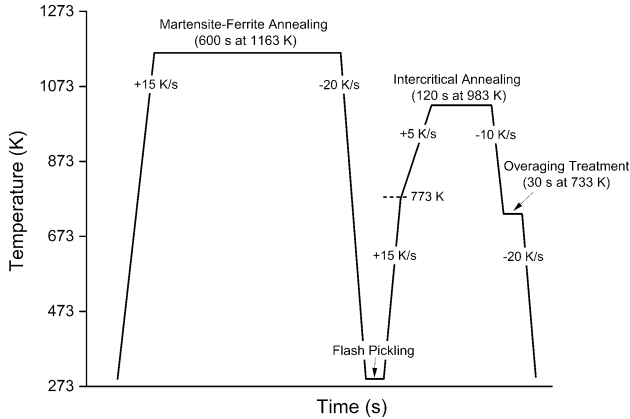


Fig. 2—Schematic thermal profile for the experimental steel.

CGL are reducing to Fe but oxidizing to other alloying elements added to obtain the desired microstructure and mechanical properties. The thermodynamically stable oxides that form during annealing can preclude successful reactive wetting by the molten galvanizing bath metal by preventing the dissolved Al in the bath from reacting with the substrate Fe to form the $Fe_2Al_{5-x}Zn_x$ interfacial layer required for an adherent, defect-free, and formable coating.^[12–14,18–23]

Despite these challenges, several authors have reported successful reactive wetting of Mn-, Si-, and Al-containing AHSSs provided the external oxides that were of an appropriate chemistry, thickness, and morphology.^[12–15,24–30] As proposed by Suzuki *et al.*,^[31] maintaining an alloy Si/Mn ratio ≤ 0.5 can promote the formation of MnO and avoid film-type SiO_2 (which is particularly problematic for reactive wetting^[18–20,32,33]). In addition, it has been shown that MnO can be aluminothermally reduced during immersion in the bath metal,^[19,26,28,34] although the thickness should be limited to 80 nm for typical immersion times.^[28] It is also known that wide spacing of oxide nodules can facilitate reactive wetting,^[12,25,27,34] as can infiltration of bath metal through cracks at the oxide/substrate

interface.^[12,15,27,34] In addition, it has been established that selective oxidation kinetics can be retarded by adding surface active elements such as Sn,^[35–39] Sb,^[35] or Bi.^[40] Moreover, a relatively high process atmosphere pO_2 can be used to suppress external oxidation and can promote the internal oxidation of alloying elements, thereby increasing the area fraction of substrate available for reactive wetting.^[14,15,39,41–43] These efforts have generally been focused on 1G AHSS grades, although recently these approaches were successfully employed by Pourmajidian and McDermid in their selective oxidation and reactive wetting studies on 0.1C-6Mn-2Si-(0-0.05)Sn (wt pct) model alloys.^[16,34,37,39]

However, the majority of work published thus far on medium-Mn 3G AHSSs has generally focused on the selective oxidation occurring during a single annealing cycle. Furthermore, it has been shown in previous work by the present authors^[10] and several other researchers^[5–9,44–46] that a two-stage heat treatment process results in improved mechanical properties relative to a one-stage intercritical annealing cycle for these alloys. The first stage is a high-temperature austenitization anneal designed to create a martensitic microstructure and the second stage comprises an intercritical annealing treatment for austenite reversion and overaging at 733 K for CGL processing compatibility. Depending on substrate chemistry and choice of annealing parameters, the resulting microstructure contains significant (0.2 TO 0.4) volume fractions of ultra-fine grained lamellar-retained austenite in a partially decomposed martensitic matrix, along with some ferrite. As such, robust mechanical properties within the 24,000 MPa pct \leq UTS \times TE \leq 40,000 MPa pct target window for 3G AHSS (as defined by Matlock and Speer^[1,2]) can be achieved. However, additional work must be done to document the selective oxidation of substrate alloying elements during this process. The chemical and morphological characterization of these surface structures is a critical component in overcoming the current knowledge gap of appropriate annealing parameter selection to successfully galvanize medium-Mn 3G AHSS substrates.

To this end, the objective of this work is to determine the effects of process atmosphere pO_2 on the selective oxide chemistry, morphology, and distribution for a prototype 0.15C-5.6Mn-1.9Al-1.1Si (wt pct) alloy as it is thermally processed through a two-stage CGL-compatible annealing cycle with intermediate flash pickling. Within the context of the overall CGL process, the surfaces produced must be such that they are compatible

Table II. Compositions of the 95N₂-5H₂-xH₂O (vol pct) Process Atmospheres at the MF and IA Annealing Temperatures. Process Atmosphere pO₂ Values were Calculated Using the FREED Thermodynamic Database^[47]

Annealing Stage (Temperature)	Atmosphere ID	Dew Point (K)	pH ₂ O/pH ₂	pO ₂ (atm)
MF (1163 K)	- 30 °C dp	243	9.98×10^{-3}	3.27×10^{-21}
	- 10 °C dp	263	5.62×10^{-2}	1.04×10^{-19}
	+ 5 °C dp	278	1.71×10^{-1}	9.62×10^{-19}
IA (983 K)	- 30 °C dp	243	9.98×10^{-3}	2.71×10^{-25}
	- 10 °C dp	263	5.62×10^{-2}	8.58×10^{-24}
	+ 5 °C dp	278	1.71×10^{-1}	7.96×10^{-23}

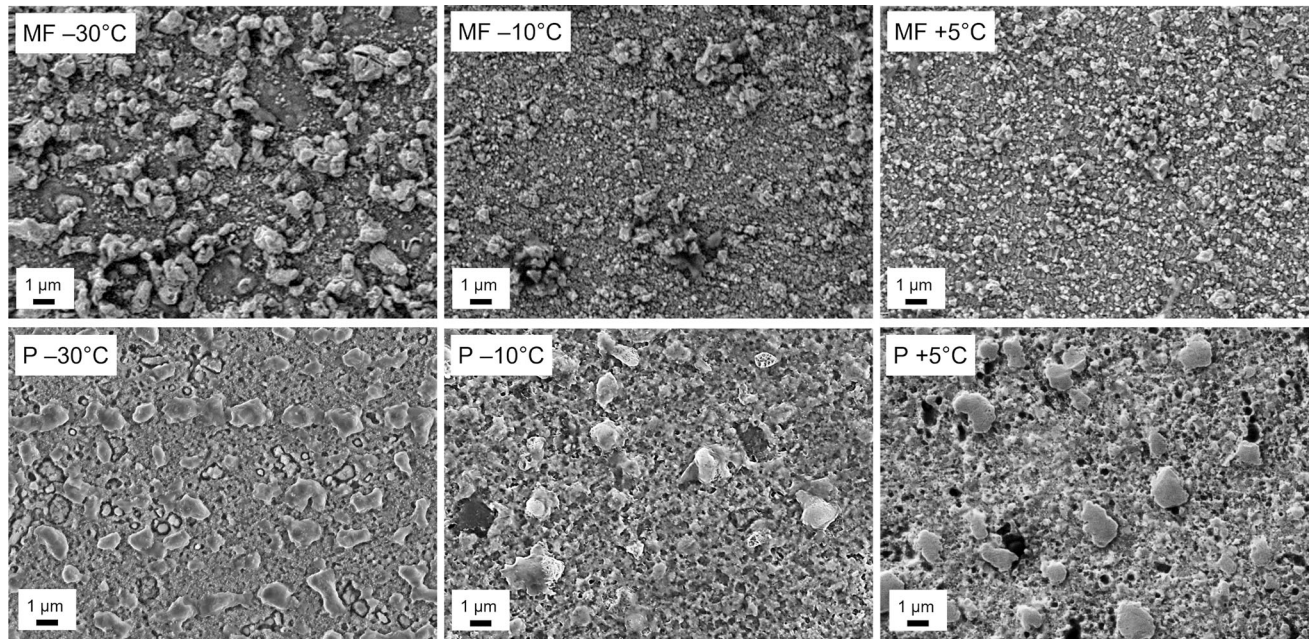


Fig. 3—SEM images showing external oxidation and Fe nodule extrusion on samples after MF annealing before and after pickling (P). The temperature indicated is the process atmosphere dew point used during the MF anneal.

with the reactive wetting process required to form integral, adherent Zn-based coatings.

II. EXPERIMENTAL PROCEDURE

The experimental substrate used in this investigation was fabricated at United States Steel Research (Munhall) via vacuum melting, slab casting, hot rolling, simulated coiling, edge trimming, surface grinding, and cold rolling, as shown in Figure 1 with additional details. The chemical composition of the substrate, as determined via combustion analysis and inductively coupled optical emission spectroscopy, is shown in Table 1. The substrate was received in the cold-rolled condition with a microstructure comprising tempered martensite and ferrite. The strip thickness was 1.2 mm. It was shown by the present authors that 3G AHSS mechanical property targets (*i.e.*, YS = 844 MPa, UTS = 1209 MPa, TE = 23 pct, UTS × TE = 27,800 MPa pct) were realized by this experimental steel after it had been thermally processed through the two-stage annealing treatment schematically shown in

Figure 2.^[10] The process atmosphere oxygen partial pressure (pO₂) values employed during each annealing stage are documented in Table II.

Coupons measuring 20 mm (TD) × 50 mm (RD) were cleaned in a 353 K 2 vol pct NaOH_(aq) solution, rinsed in deionized water, rinsed in ethanol, and dried with warm air. The coupons were polished on one side using 4,000 grit SiC paper to minimize the effects of cold-rolling surface texture on subsequent analyses. All samples were cleaned with acetone wipes immediately prior to annealing. Annealing cycles were performed in the McMaster Galvanizing Simulator (MGS, Iwatani-Surtec), according to Figure 2, Table II, and additional details documented in a previous publication by the present authors.^[10] A 0.5 mm type K thermocouple was welded directly to the samples to control the thermal cycle.

Three sets of samples were prepared in order to isolate the effects of process atmosphere pO₂ and annealing stage on selective oxidation: (1) austenitization anneal resulting in a martensite-ferrite microstructure (MF) only; (2) austenitization anneal + flash pickling treatment (P); and (3) austenitization anneal + flash

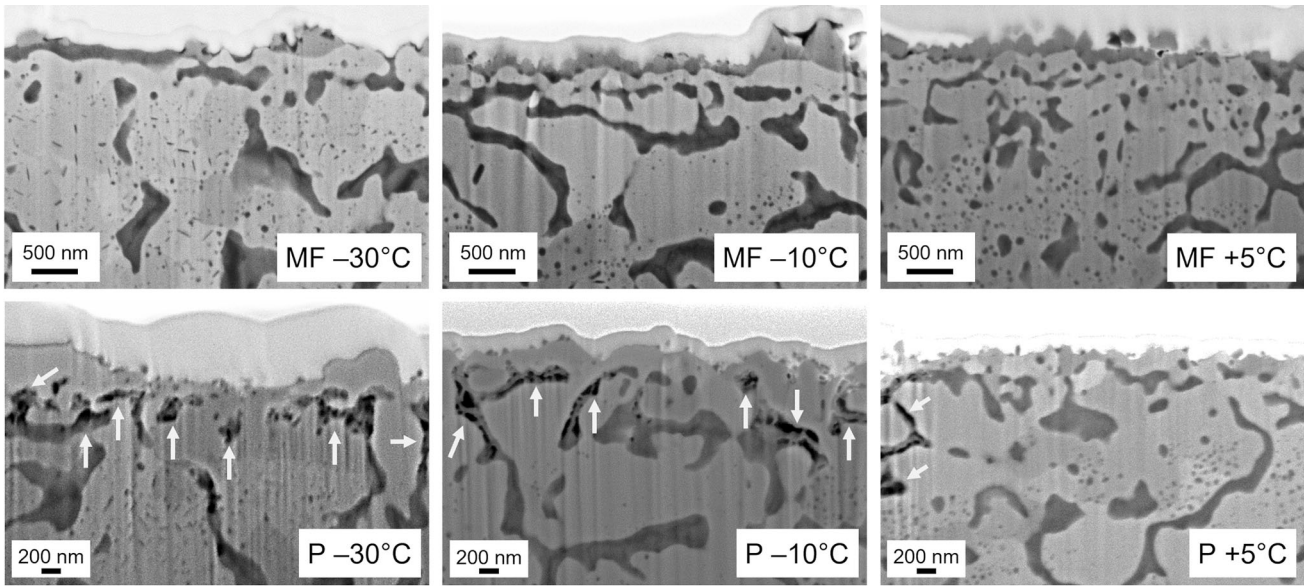


Fig. 4—SEM images of FIB-prepared trench cuts showing internal and external oxides on samples after MF annealing and after pickling. Arrows indicate selectively dissolved near-surface internal oxide structures as a result of flash pickling. Note that the temperature labels on the micrographs are the process atmosphere dew points used for the MF anneal with the corresponding as-pickled surfaces.

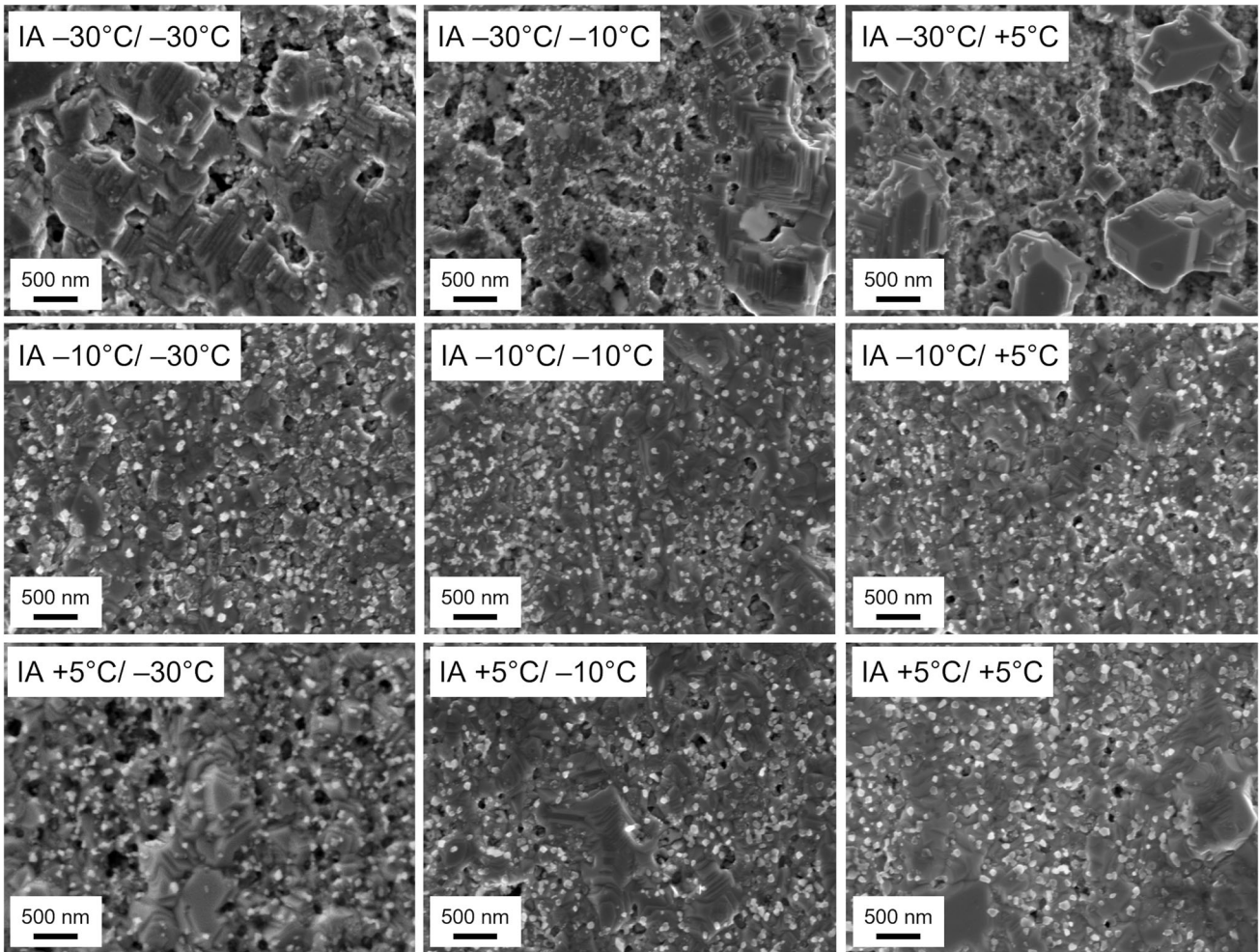


Fig. 5—SEM images showing the selectively oxidized surfaces after intercritical annealing. The temperature labels on the micrographs are the process atmosphere dew points used for the MF and IA anneals, respectively.

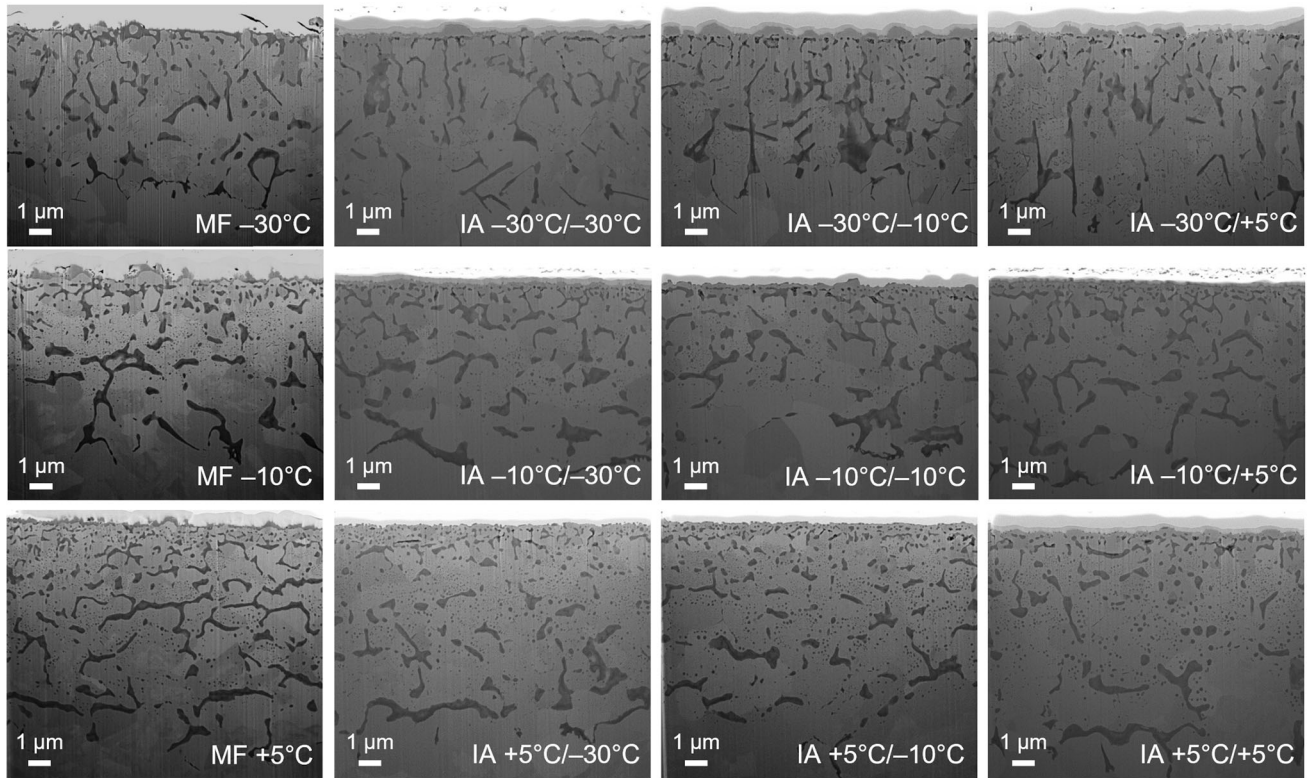


Fig. 6—SEM images of the FIB-prepared trench cuts showing a wider view of the internal and external selective oxides before and after intercritical annealing.

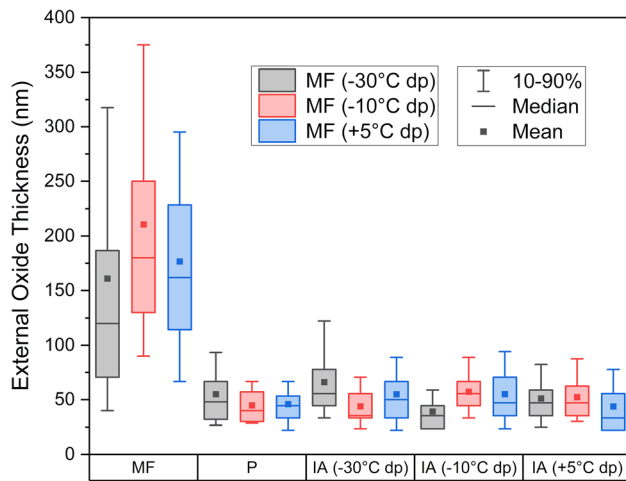


Fig. 7—Box-and-whisker plot showing the distribution of external oxide thickness as a function of process atmosphere during each annealing step. The box encloses 25 to 75 pct of the data and the whiskers enclose 10 to 90 pct of the data.

pickling + intercritical anneal (IA). Samples are identified with the dew point used for the MF and, if applicable, IA stages—e.g., MF -30°C denotes a sample austenitized in a -30°C dew point atmosphere and IA $-30^{\circ}\text{C}/+5^{\circ}\text{C}$ denotes the same MF treatment subsequently intercritically annealed in a $+5^{\circ}\text{C}$ dew

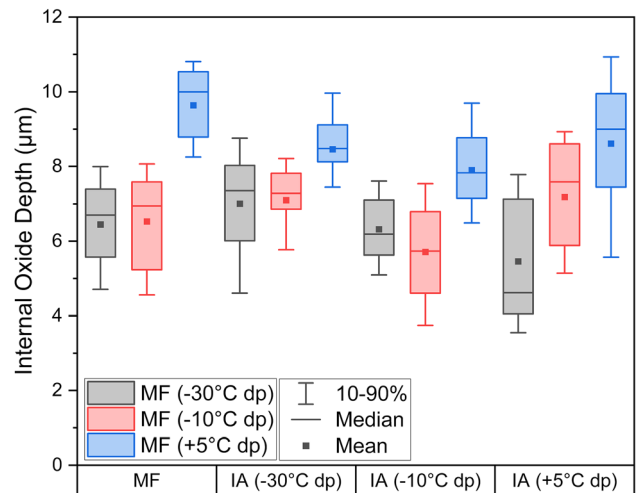


Fig. 8—Box-and-whisker plot showing the distribution of internal oxidation depth as a function of process atmosphere dew point during each annealing step. The box encloses 25 to 75 pct of the data and the whiskers enclose 10–90 pct of the data.

point atmosphere. Flash pickling (P) was performed by lightly agitating the samples for 60 s in a 303 K solution comprising 64.5 mL deionized water + 59.6 mL hydrochloric acid + 0.25 g hexamethylenetetramine, agitating in room-temperature deionized water for 20 s, rinsing with ethanol, and drying in warm air.

Table III. Identification of Surface Oxide Species Present After MF and P Treatments, via Measured XPS Binding Energies

Sample	Measured XPS Binding Energies (eV)			Oxide Species Identified
	Al 2p	Mn 2p _{3/2}	Si 2p	
MF – 30 °C dp	73.8	640.4	101.8	Al ₂ O ₃ ^[49,50,52]
MF – 10 °C dp	74.0	640.8	101.7	MnAl ₂ O ₄ ^[50,53]
MF + 5 °C dp	73.6	640.7	101.4	Mn ₂ SiO ₄ ^[53] MnO ^[48,52]
P – 10 °C dp	74.4	641.5	101.6	Al ₂ O ₃ ^[49,50,52] MnAl ₂ O ₄ ^[50,53] Mn ₂ SiO ₄ ^[53]

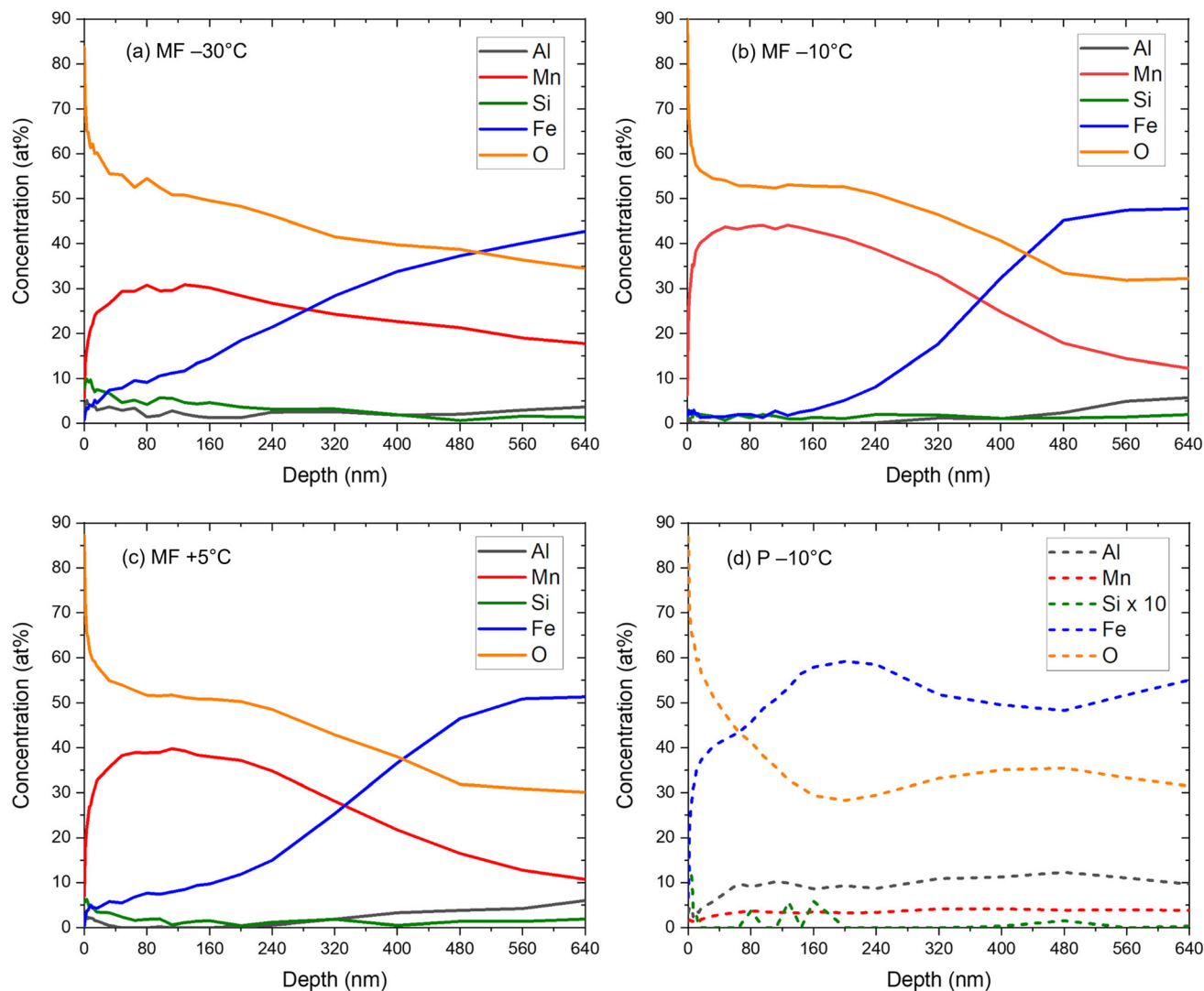


Fig. 9—XPS elemental depth profiles for Al, Mn, Si, Fe, and O concentrations for (a) MF – 30 °C dp, (b) MF – 10 °C dp, (c) MF + 5 °C dp, and (d) P – 10 °C dp.

The spatial distribution and morphology of the external oxides were documented using a Zeiss NVision 40 dual-beam SEM/FIB operated in SEM mode. The FIB was used to prepare two 15 μm-wide trenches per sample perpendicular to the steel surface such that SEM

images were acquired from the external and internal oxides in the cross section. The external oxides in the area of interest were protected during Ga⁺-ion milling by first depositing a layer of W onto the surface. The external oxide thickness and internal oxidation depth

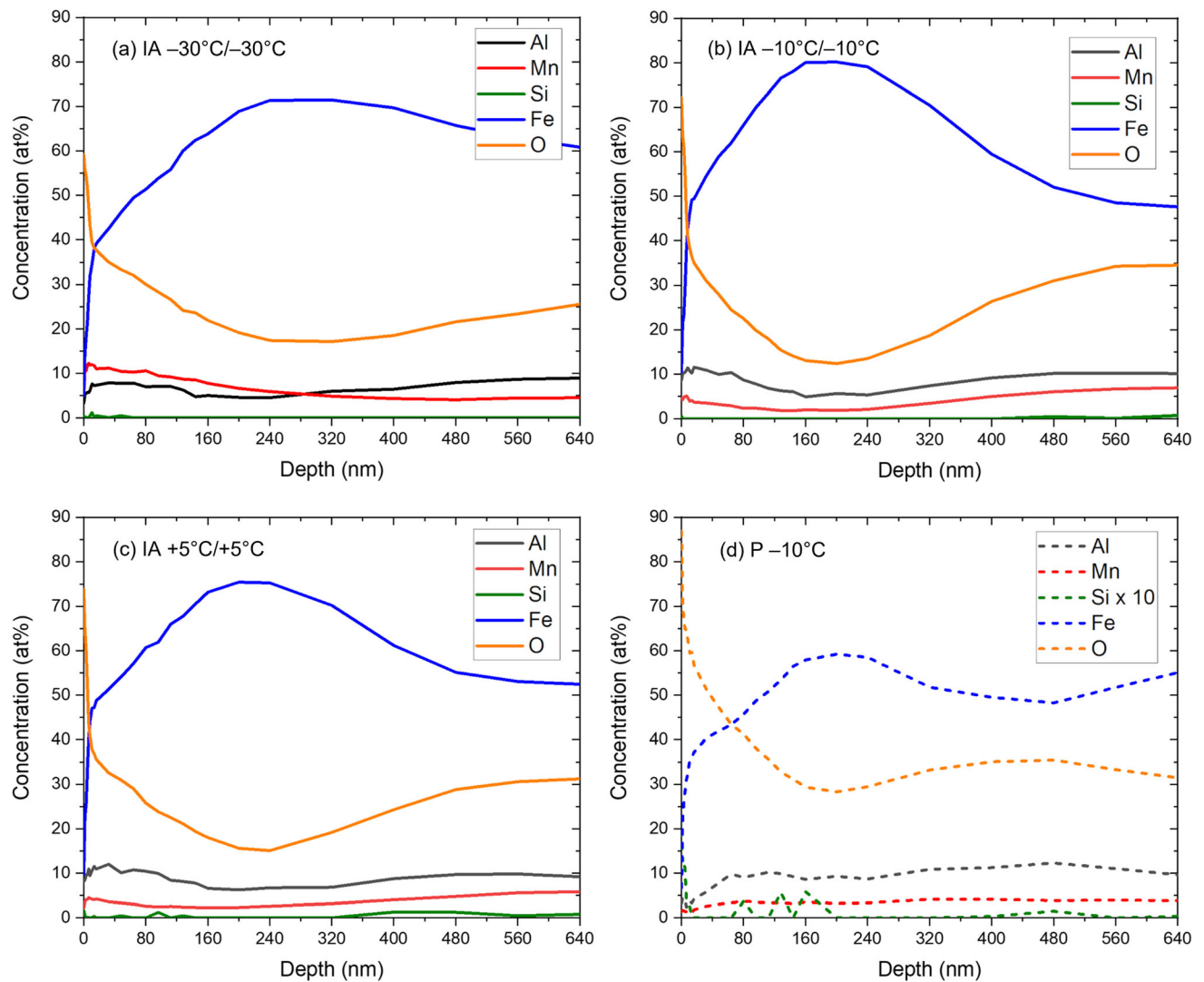


Fig. 10—XPS elemental depth profiles for Al, Mn, Si, Fe, and O concentrations for the combined MF/IA heat treatments as a function of process atmosphere dew point (a) $-30\text{ }^{\circ}\text{C}/-30\text{ }^{\circ}\text{C}$ dp, (b) $-10\text{ }^{\circ}\text{C}/-10\text{ }^{\circ}\text{C}$ dp, (c) $+5\text{ }^{\circ}\text{C}/+5\text{ }^{\circ}\text{C}$ dp, and (d) P $-10\text{ }^{\circ}\text{C}$ dp.

were measured using ImageJ 1.52a software on tilt-corrected SEM images. Per the methodology described by Pourmajidian and McDermid,^[37] at least 150 measurements were taken from each trench utilizing a grid to ensure unbiased sampling. The external oxide thickness and internal oxidation depth data are presented using box-and-whisker plots with the box showing the sample mean, median, and interquartile range with the whiskers encompassing the 10–90th percentiles.

Elemental depth profiles were acquired via X-ray photoelectron spectroscopy (XPS) using a PHI Quantera XSM XPS equipped with an Al $K\alpha$ X-ray source (1487.7 eV) and a hemispherical detector. The take-off angle was 45° and the spot size was $100\text{ }\mu\text{m}$. Ar sputtering was performed on a $2 \times 2\text{ mm}^2$ area and spectra were acquired with a pass energy of 140 eV and a step size of 0.25 eV. Data processing was performed

using MultiPak 6.0 software. The spectra were calibrated using the metallic iron binding energy of 706.62 eV and are considered accurate to within ± 0.1 eV. Depth measurements are considered to be accurate within 10 pct of the recorded sputtering depth.

Cross sections from selected samples were prepared for transmission electron microscopy (TEM) via FIB milling. High-resolution scanning transmission electron microscopy (HR-STEM) micrographs were acquired using a Thermo Scientific Talos 200X TEM operated at 200 keV or a FEI Titan 80–300 HB TEM operated at 300 keV in STEM mode. Electron energy loss spectroscopy (EELS) was performed to determine the elemental distribution and chemistry of the external and internal oxides. The spectra were obtained using a CMOS (Talos 200X) or Gatan Quantum GIF (Titan 80–300 HB) detector and the elemental maps were

Table IV. Identification of Surface Oxide Species Present After Intercritical Annealing Treatments via Measured XPS Binding Energies

IA Sample	Measured XPS Binding Energies (eV)			Oxide Species Present
	Al 2p	Mn 2p _{3/2}	Si 2p	
- 30 °C/- 30 °C dp	74.2	641.0	101.6	Al ₂ O ₃ ^[49,50,52]
- 10 °C/- 10 °C dp	74.3	641.4	101.4	MnAl ₂ O ₄ ^[50,53]
+ 5 °C/ + 5 °C dp	74.1	641.0	101.5	Mn ₂ SiO ₄ ^[53] MnO ^[48,52]

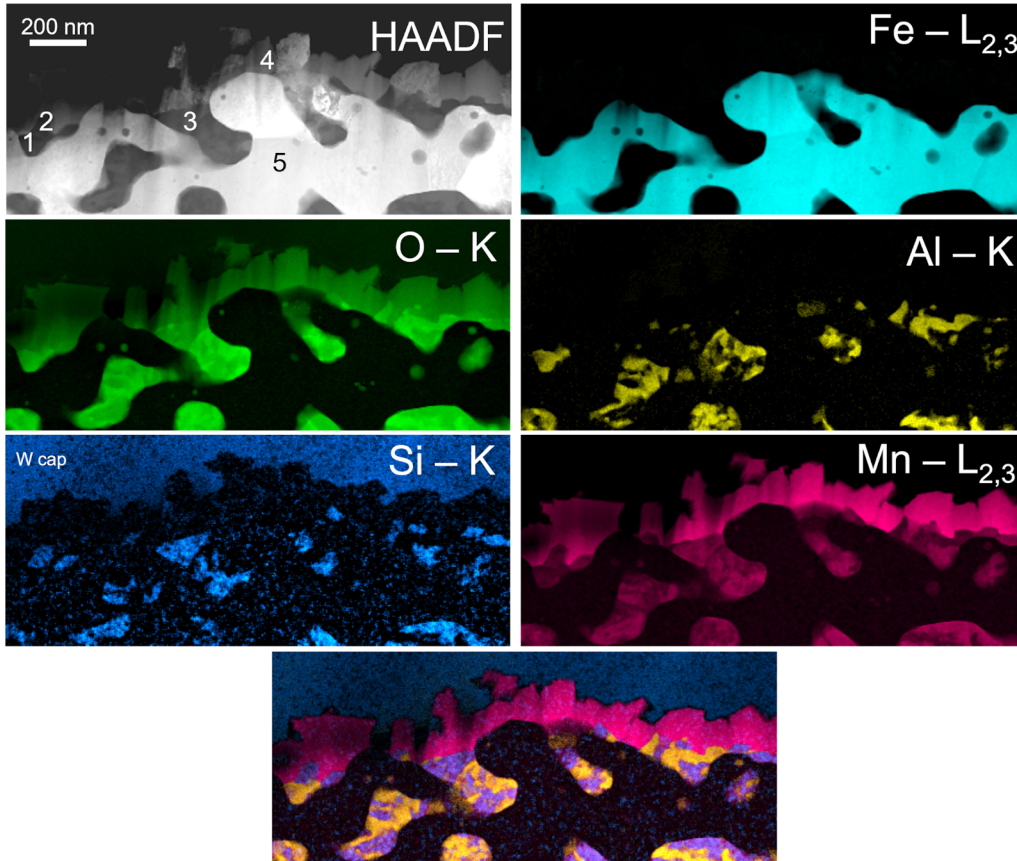


Fig. 11—HAADF image and EELS elemental maps of Fe, O, Al, Si, and Mn for the selectively oxidized MF - 10 °C dp surface. A composite map of Al, Si, and Mn is also included.

constructed using Digital Micrograph v3.43 software.

III. RESULTS

SEM images showing the surfaces resulting from MF annealing and after pickling (P) are shown in Figure 3. Figures 3(a) through (c) show that, after MF annealing, extensive external oxidation was observed irrespective of the process atmosphere dew point employed. The nodular external oxides were dispersed among extruded Fe nodules. Figures 3(d) through (f) show that the pickling treatment was effective at removing most of the external oxides, with dispersed nodules measuring tens of nm remaining. The pickled surfaces were textured due

to the presence of the extruded Fe nodules and the dissolution of oxides into the sub-surface.

FIB-prepared trench cuts were prepared from the samples in Figure 3 and are shown in Figure 4, where the cross sections through the as-annealed surfaces are shown in (a through c) and the pickled surface cross sections in (d through f). These images show that the flash pickling treatment was effective in removing most of the external oxides, leaving behind only dispersed nano-scale oxide nodules. It can also be seen that some of the near-surface internal oxides were selectively dissolved during flash pickling.

SEM images showing the surfaces after intercritical annealing are shown in Figure 5. Dispersed and discrete nodular nano-scale oxides were present after annealing

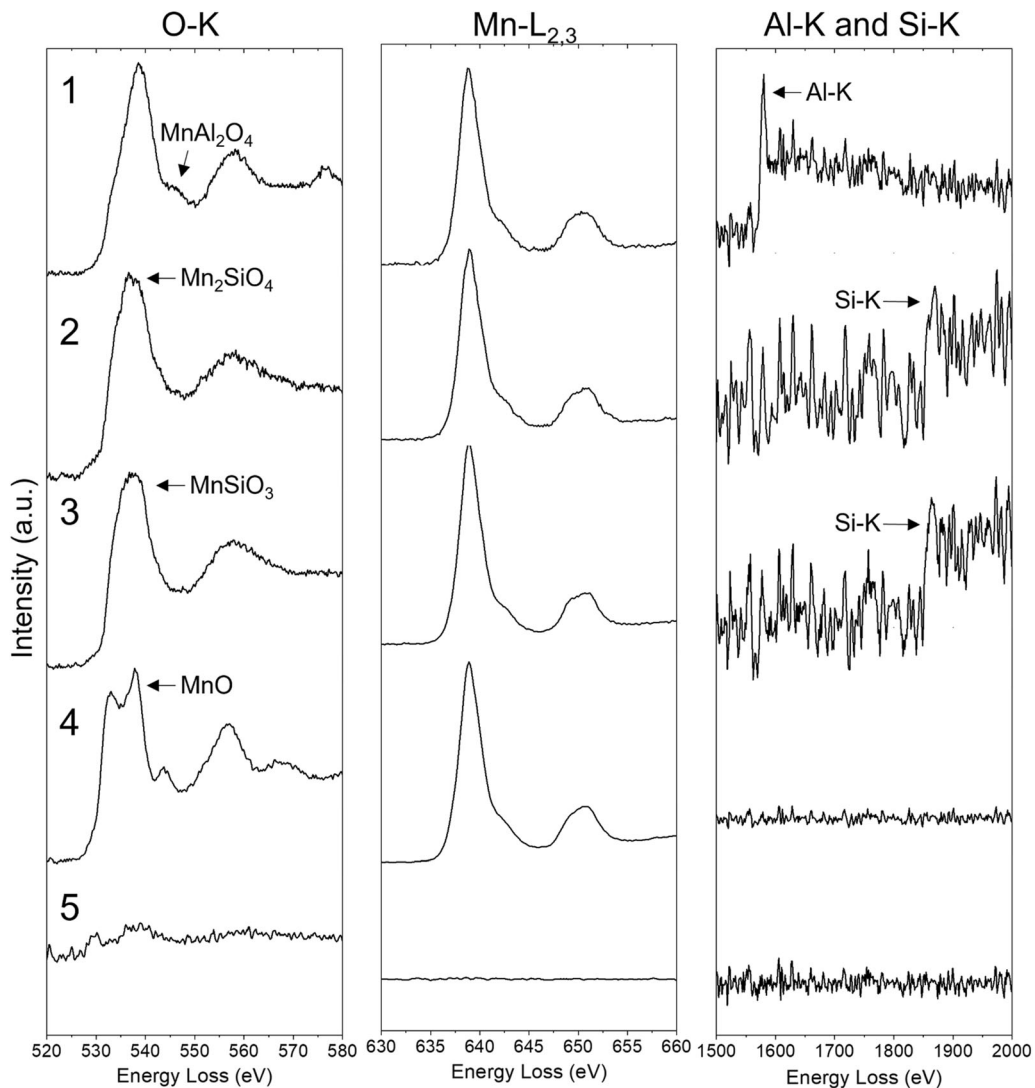


Fig. 12—EELS spectra showing the O-K, Mn-L_{2,3}, Al-K, and Si-K edges from the numbered regions in Fig. 11 (MF -10 °C dp).

for all process atmosphere dew point combinations explored. Moreover, the extruded Fe nodules present on the as-pickled surfaces were preserved, as were the pores from selective oxide dissolution during pickling. The FIB trench cut images in Figure 6 present a wider view of the trenches for further elucidation of the overall depth of internal oxidation, which can be seen to comprise several microns.

Box-and-whisker plots showing the measured external oxide thickness and internal oxidation depth as a function of annealing stage are shown in Figures 7 and 8, respectively. Examination of Figure 7 will show that the mean external oxide thickness after the MF treatment was between 160 and 210 nm, irrespective of the process atmosphere dew point employed. After flash pickling, the mean external oxide thickness decreased to approximately 50 nm, and did not increase significantly during intercritical annealing, irrespective of process atmosphere pO₂. In addition, examination of Figure 8 will show that the depth of internal oxidation did not increase significantly from the MF to the IA condition.

This suggests that the available near-surface solutes were selectively oxidized during the MF annealing step and that there was insufficient time for solute diffusion for further oxide growth during intercritical annealing.

High-resolution XPS scans of the MF - 30 °C dp, MF - 10 °C dp, MF + 5 °C dp, and P - 10 °C dp sample were obtained in order to identify the chemical species present on their surfaces. The measured Al 2p, Mn 2p_{3/2}, and Si 2p binding energies are shown in Table III. From Table III, it can be seen that the Al 2p, Mn 2p_{3/2}, and Si 2p binding energies did not vary significantly among the samples, indicating that the documented external oxide species was independent of the process atmosphere dew point employed during the MF anneal. The binding energies correlate to MnO, Mn₂SiO₄, MnAl₂O₄, and Al₂O₃.^[48–53]

XPS was also used to acquire elemental depth profiles from the MF - 30 °C dp, MF - 10 °C dp, and MF + 5 °C dp samples to ascertain the segregation of Mn, Si, and Al towards the surface and approximate the thickness of the external oxide layer. These are shown in

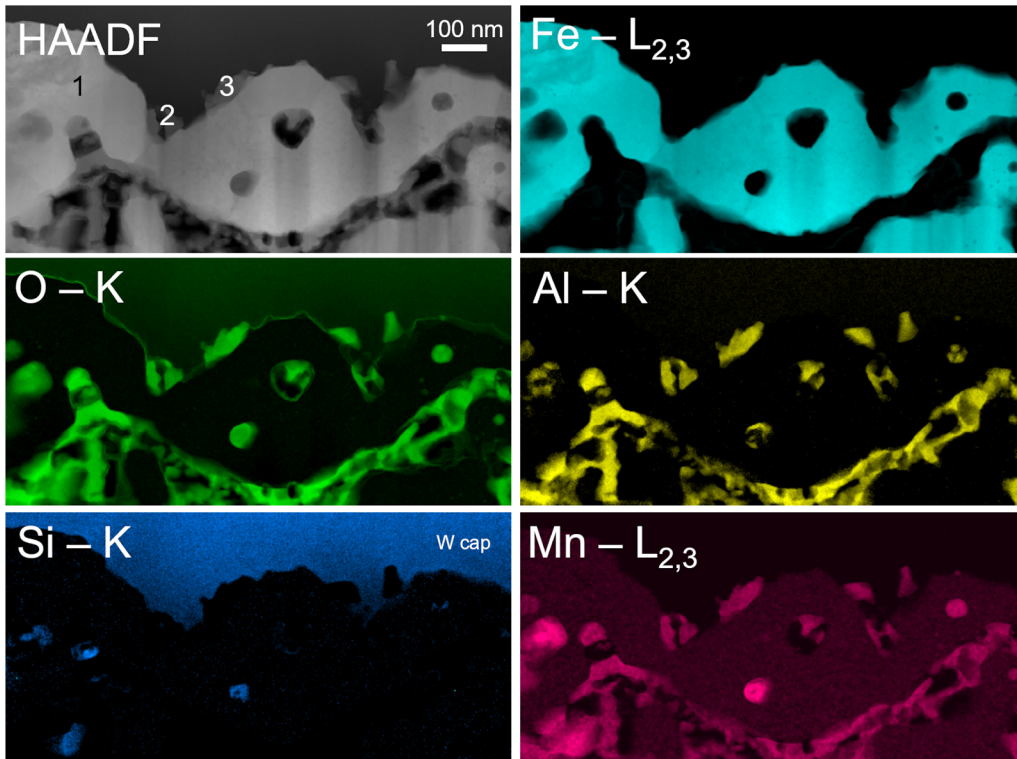


Fig. 13—HAADF image and EELS elemental maps of Fe, O, Al, Si, and Mn showing the external oxides remaining after flash pickling (P – 10 °C dp sample).

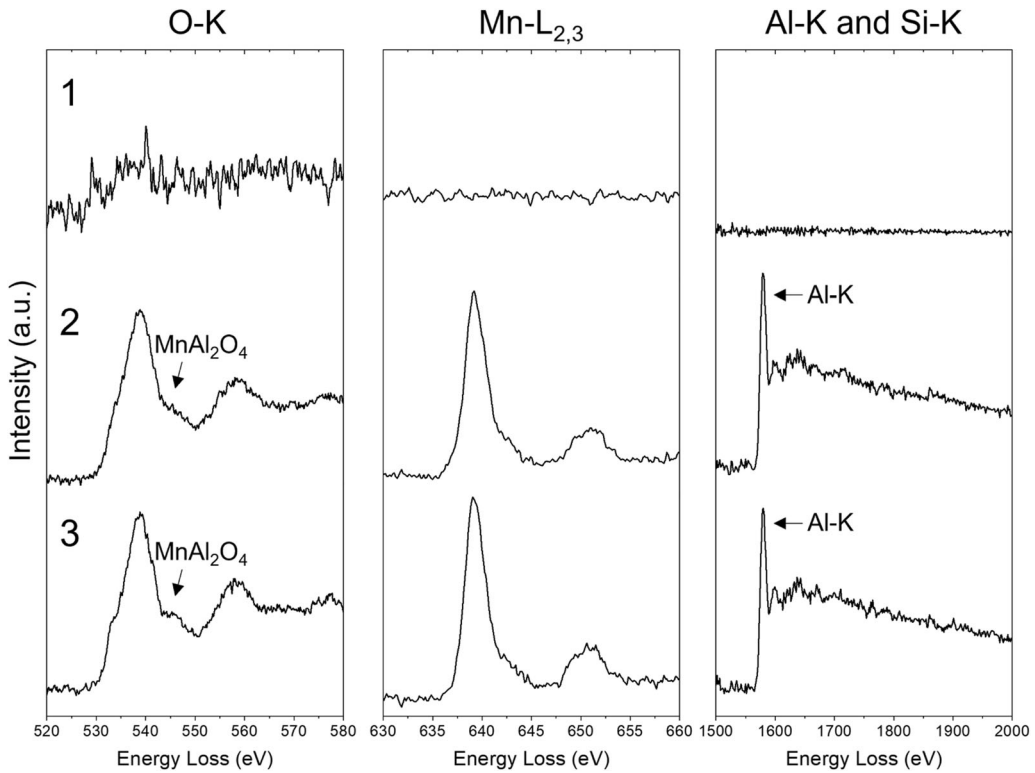


Fig. 14—EELS spectra showing the O-K, Mn-L_{2,3}, Al-K, and Si-K edges from the numbered regions in Fig. 13 (P – 10 °C dp).

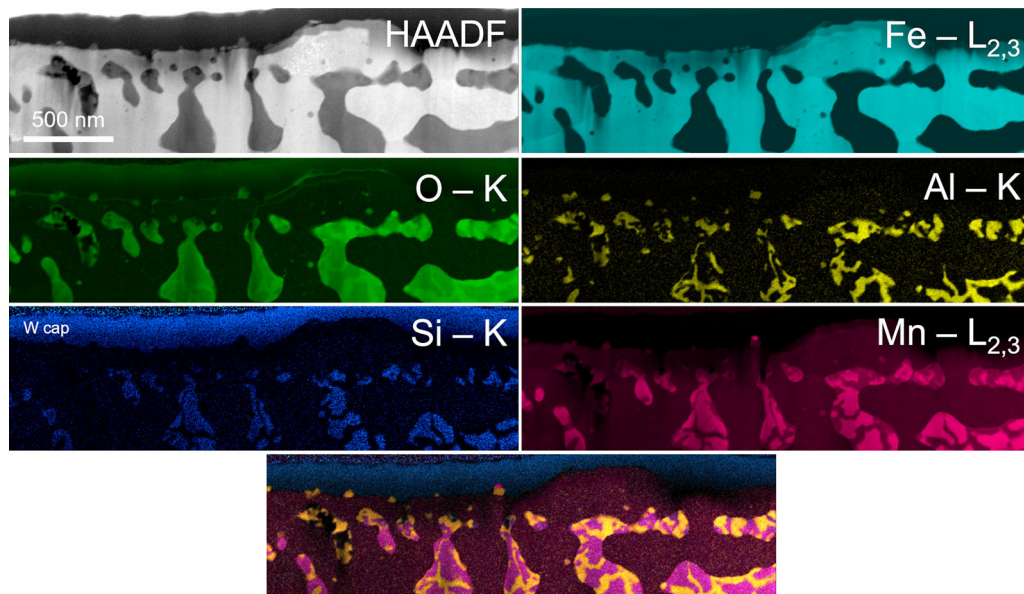


Fig. 15—Representative HAADF image and EELS elemental maps of Fe, O, Al, Si, and Mn showing the selective oxides remaining after intercritical annealing (IA – 10 °C/– 30 °C dp sample pictured). A composite map of Al, Mn, and Si is also included.

Figure 9 in addition to the XPS elemental depth profiles of the P –10 °C sample, obtained to quantify the effectiveness of the pickling treatment. The depth profiles for the MF –30 °C dp, MF –10 °C dp, and MF + 5 °C dp samples [Figures 9(a) through (c)] are similar and show significant enrichment of O and Mn at the surface. Moreover, the gradual increase in the Fe profile suggests the existence of a non-planar oxide–substrate interface. The elemental depth profiles for the P –10 °C dp sample [Figure 9(d)] show that the external selective oxide layer was effectively removed by the pickling treatment and correlates well with the surface morphology documented in Figure 4 and the external oxide measurements presented in Figure 8. Moreover, Mn and Si levels were depleted relative to the unpickled MF samples, corroborating the SEM images (Figures 3 and 4) showing the dissolution of some near-surface oxide species in the pickled samples.

Mn, Si, and Al XPS depth profiles were acquired for selected intercritically annealed samples and are shown in Figure 10, in addition to the P – 10 °C dp sample presented in Figure 9(d) to facilitate comparison by the reader. As was the case for the P – 10 °C dp sample, the three IA samples exhibited rapid increases in their respective Fe curves at shallow (< 20 nm) depths, suggesting that there was no significant additional external oxidation during intercritical annealing. This corroborates the SEM images in Figure 5, which show nodular and dispersed nano-scaled selective oxides on the IA samples. In the three IA cases, the Si levels were depleted relative to the bulk concentration of 2 at. pct, likely due to the formation of Si-containing oxides during the MF annealing step and subsequent dissolution of these species by flash pickling.

High-resolution XPS analysis was performed to elucidate the effects of process atmosphere (for both annealing stages) on the external oxide chemistry. Table IV shows the Al 2p, Mn 2p_{3/2}, and Si 2p XPS-binding energies obtained from the sample surfaces, in addition to the proposed oxide species present. In all cases, the experimentally determined binding energies for Al 2p align closely with the reported values for Al₂O₃^[49,50,52] and MnAl₂O₄^[50,53]. The measured binding energies for Si 2p match closely with that of Mn₂SiO₄^[53]. This suggests that SiO₂ (reported binding energy of 103.3^[52] or 103.9 eV^[49,51]) formation was avoided, which is promising for future galvanizing studies since the film-like morphology of SiO₂ is known to be deleterious to reactive wetting.^[18–20,32,33] It should be noted, however, that the low atomic fraction of Si obtained for all samples (Figure 10) suggests that the coverage of Mn₂SiO₄ is likely to be insignificant relative to elemental Fe and other external oxide species. Furthermore, the experimentally determined binding energies for Mn 2p_{3/2} do not align as closely with a single reference value. This, in combination with the relative broadness of the peaks, suggests that Mn was present in multiple oxide states. It can be deduced from the aforementioned Al 2p and Si 2p peak information that Mn was present in the form of MnAl₂O₄^[50,53] and Mn₂SiO₄^[53] in addition to MnO.^[50,52]

The morphology and chemistry of the selective oxides formed during each annealing stage were determined using STEM-EELS elemental mapping and spectral analysis. Based on the aforementioned XPS analysis, the MF – 10 °C dp sample was selected for STEM–EELS analysis of the oxides formed during the MF annealing step. A lift-out of the P – 10 °C dp sample was also

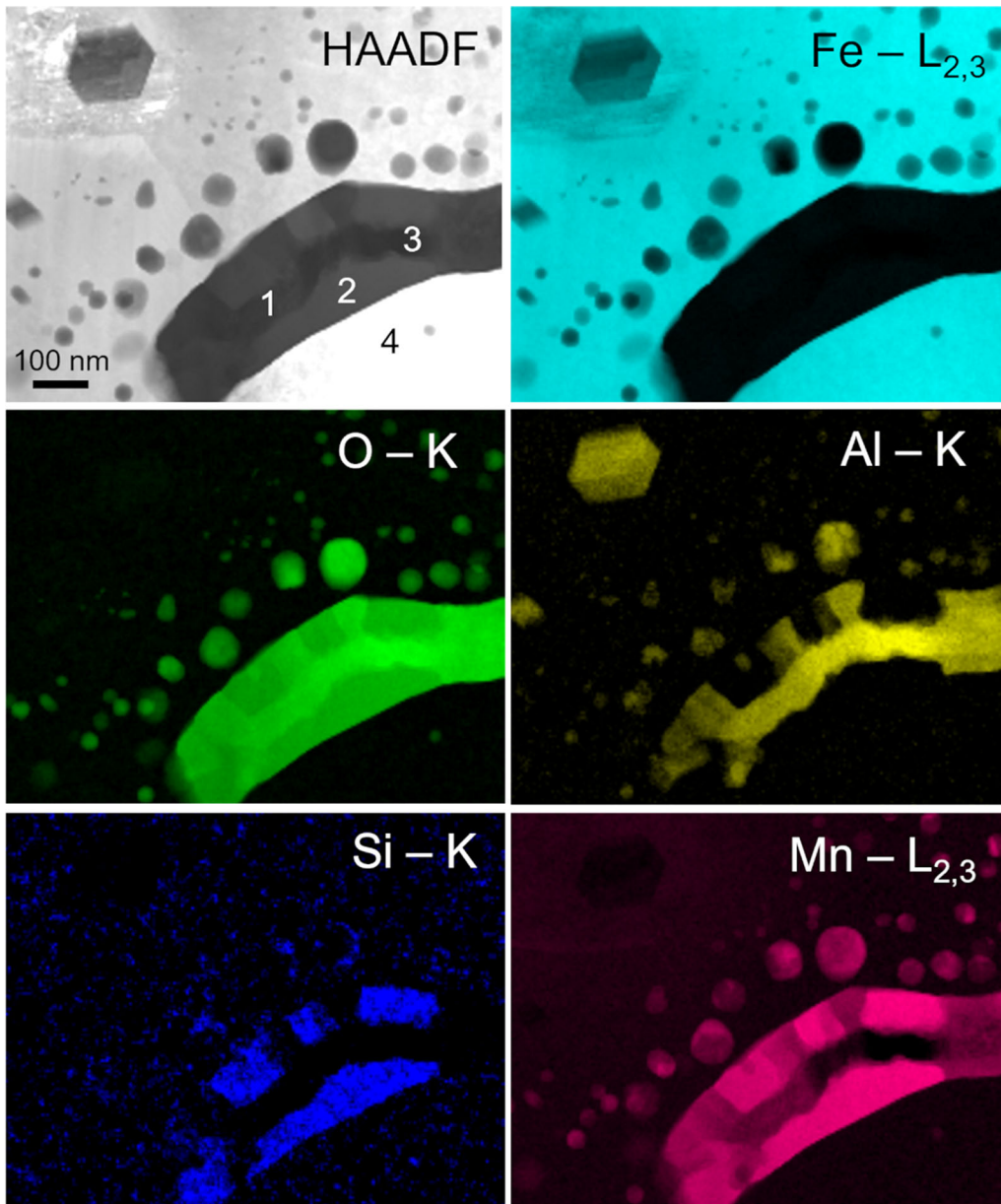


Fig. 16—HAADF image and EELS elemental maps of Fe, O, Al, Si, and Mn showing a representative grain boundary oxide structure from the MF - 10 °C dp sample.

prepared to examine the effects of flash pickling on the surface and near-surface microstructures. Subsequently, STEM-EELS analysis of the IA - 10 °C/- 30 °C dp, IA - 10 °C/- 10 °C dp, and IA - 10 °C/ + 5 °C dp samples was performed to determine the effects of intercritical annealing on the selective oxides formed relative to those observed for the P - 10 °C sample.

A. Evolution of External Oxide Structures

EELS elemental maps of the MF - 10 °C dp surface are shown in Figure 11 with EELS spectra from selected locations documented in Figure 12. A compact and layered oxide structure was observed. The largest proportion of the external oxide species observed

(Region 4 in Figure 11) was a compact layer of Mn oxide nodules approximately 100 to 200 nm thick, which was identified as MnO based on the EELS spectra^[54] in Figure 12. In some areas, these MnO nodules grew directly on top of the Fe substrate; however, in other areas, MnO nodules grew on top of a discontinuous mixed Mn-Si (Regions 1 and 3 in Figure 11) and Mn-Al (Region 2 in Figure 11) oxide layer. The mixed Mn-Al and Mn-Si oxides also co-precipitated internally along grain boundaries. Based on the EELS spectra in Figure 12, these species were identified as MnAl_2O_4 , MnSiO_3 , and Mn_2SiO_4 .^[53] It is also noteworthy that spectra taken from the top 200 nm of the matrix showed no appreciable signal from Mn, Si, or Al, as shown in the spectra from Region 5 in Figure 12,

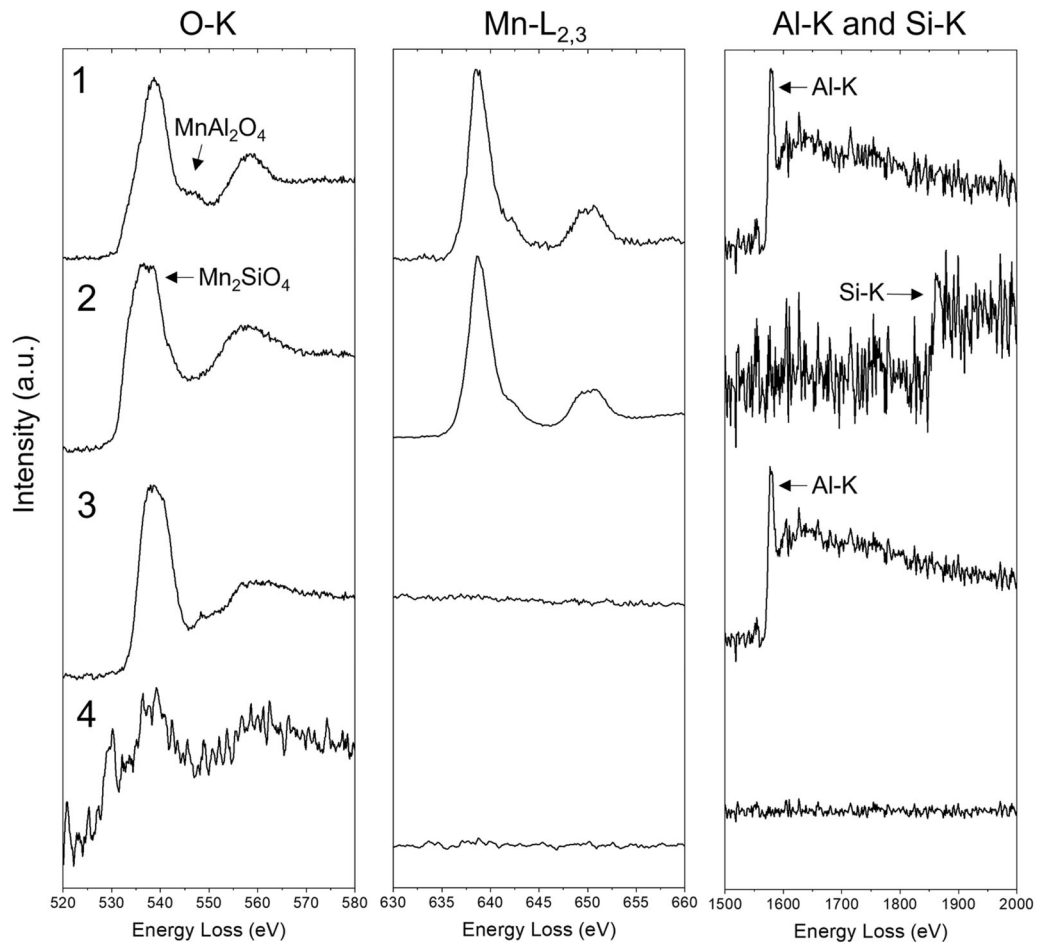


Fig. 17—EELS spectra showing the O-K, Mn-L_{2,3}, Al-K, and Si-K edges from the numbered regions in Fig. 16 (MF – 10 °C dp).

indicating that the various solutes had been severely depleted in this near-surface zone.

EELS elemental maps of the P – 10 °C dp surface are shown in Figure 13, with corresponding EELS spectra from selected locations provided in Figure 14. It is evident that the pickling treatment effectively removed the surface MnO, MnSiO₃, and Mn₂SiO₄ species but left behind MnAl₂O₄^[55,56] nodules (Regions 2 and 3 in Figures 13 and 14). The holes in the near-surface internal oxide structure are due to the selective dissolution of internal Mn-Si oxides which were exposed to the pickling solution through connection to the surface. This is consistent with literature showing that MnO,^[57] MnSiO₃,^[58] and Mn₂SiO₄^[59] are soluble in hydrochloric acid solutions over a wide pH range with reasonably rapid dissolution kinetics, whereas the present authors could find no such studies published for MnAl₂O₄.

The effects of intercritical annealing on the development of external oxides on the pickled sample surfaces are shown in the STEM-EELS elemental maps for the IA – 10 °C/– 30 °C dp sample surface shown in Figure 15. This image is also representative of the IA – 10 °C/– 10 °C dp and IA – 10 °C/ + 5 °C dp samples (not pictured). From EELS spectral analysis, it was determined that the dispersed external nodular Mn-Al oxides observed on these samples were MnAl₂O₄, per

the surface of the P – 10 °C dp sample (Figure 13). This suggests that no significant external oxide growth took place during intercritical annealing, implying that the pre-immersion surface structures that would enter the galvanizing bath were the relatively clean as-pickled surfaces. Examination of Figure 15 also shows that the pores created during flash pickling were preserved during intercritical annealing.

B. Evolution of Internal Oxide Structures

Figure 16 comprises the STEM-EELS maps of grain boundary oxides observed approximately 3 μm beneath the surface of the MF – 10 °C dp sample. These grain boundary oxides formed in a core-shell morphology, with Al and Mn enrichment in the oxide core and Mn and Si enrichment in the shell. EELS spectral analysis (Figure 17) determined that the core oxides comprised Al₂O₃^[55,56] and MnAl₂O₄^[53] while the shells comprised mainly Mn₂SiO₄.^[53] These findings are similar to those documented by other authors who investigated low-alloy TRIP^[17,41,60–64] and medium-Mn^[16,34] steels containing varying amounts of Mn, Si, and Al. However, these authors described a selective oxide morphology comprising a SiO₂ core surrounded by MnSiO₃/Mn₂SiO₄ shell. In contrast, the present findings are

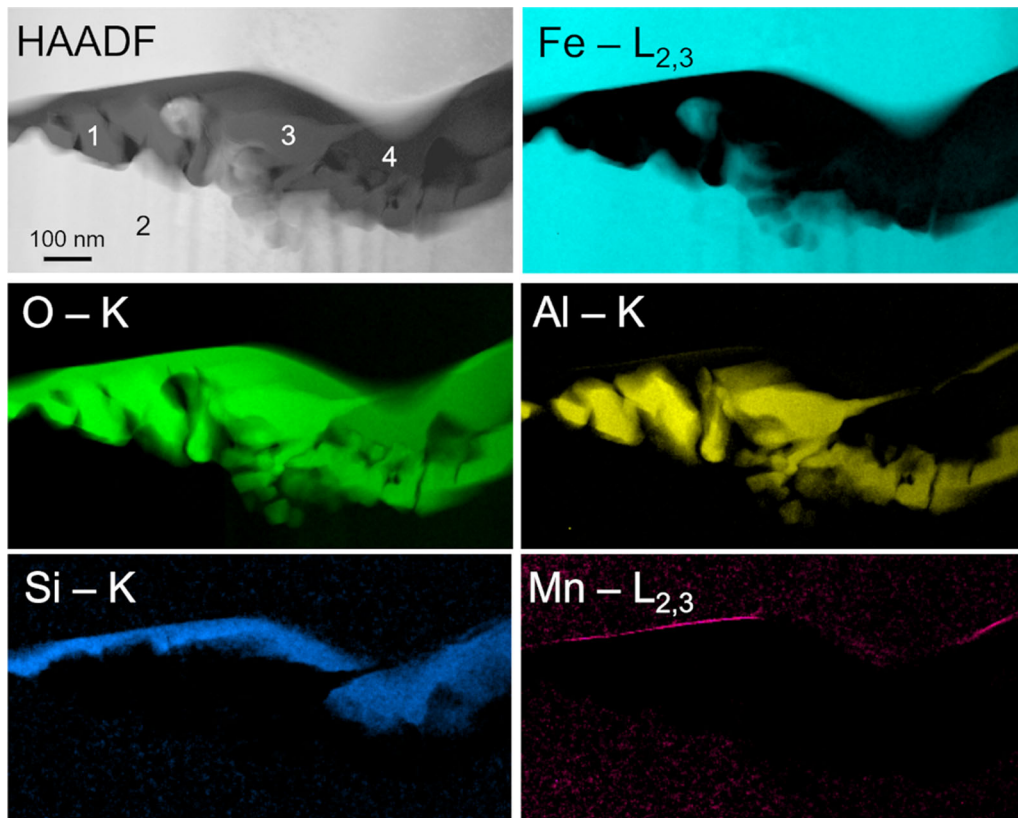


Fig. 18—HAADF image and EELS elemental maps of Fe, O, Al, Si, and Mn showing a grain boundary oxide in the deepest part of the oxide network in the MF – 10 °C dp sample.

comparable to those of Li *et al.*^[65], who found that some internal selective oxides in their 0.15C-1.55Mn-0.29Si-1.51Al-0.51Cu (wt pct) TRIP steel comprised an Al oxide core and Mn-Si oxide shell. Examination of the spectrum taken from Region 4 in Figure 17 shows that the matrix surrounding this oxide was depleted in Mn, Al, and Si.

The deepest internal oxides observed in the MF – 10 °C dp sample are typified by the STEM-EELS elemental maps shown in Figure 18. This oxide grouping was found approximately 8 μm deep into the sample and comprised a Si-rich oxide capping an Al-rich oxide, with a very thin layer of Mn oxide precipitating on the Si oxide cap. Analysis of the EELS spectra (Figure 19) confirmed that the major oxide species were SiO₂^[66,67] and Al₂O₃^[55,56] and that the local matrix was depleted in Al and Si, but contained some Mn. This suggests that the local dissolved O content was too low to selectively oxidize Mn, although the relative alloying element diffusion rates and the relatively high solubility of MnO in ferrite may have also contributed to the lack of Mn oxides. The calculated solubility products at 1163 K for the oxides of interest in pure Fe are shown in Table V.^[68–70]

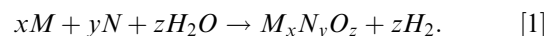
The internal oxide structures observed in the IA – 10 °C/– 30 °C dp, IA – 10 °C/– 10 °C dp, and IA – 10 °C/+ 5 °C dp samples were similar to those observed in the MF – 10 °C dp sample (Figures 16 and

18). A representative grain boundary taken from the IA – 10 °C/– 10 °C dp sample is shown in the EELS elemental maps in Figure 20 (with corresponding EELS spectra in Figure 21). Analysis of the EELS spectra showed that the shells were primarily composed of Mn₂SiO₄ and nodules of MnO precipitated on the shell (per region 4 in Figure 20).

A summary of the TEM-EELS analysis, documenting the evolution of the MF – 10 °C dp austenitization as a function of subsequent processing step, can be found in Table VI. An examination of Table VI will show that the vast majority of the selective oxidation of the ignoble alloying elements occurred during the austenitization annealing cycle and progressed in only a minor way during the subsequent intercritical, leaving the as-pickled surfaces—comprising large area fractions of near-pure, solute-depleted Fe—at the surface.

IV. DISCUSSION

In the case of typical dew point-controlled continuous galvanizing atmospheres comprising N₂-(5–20)H₂-xH₂O (vol pct), the formation of a general ternary oxide from ignoble metallic solute species *M* and *N* is provided by Eq. [1]:



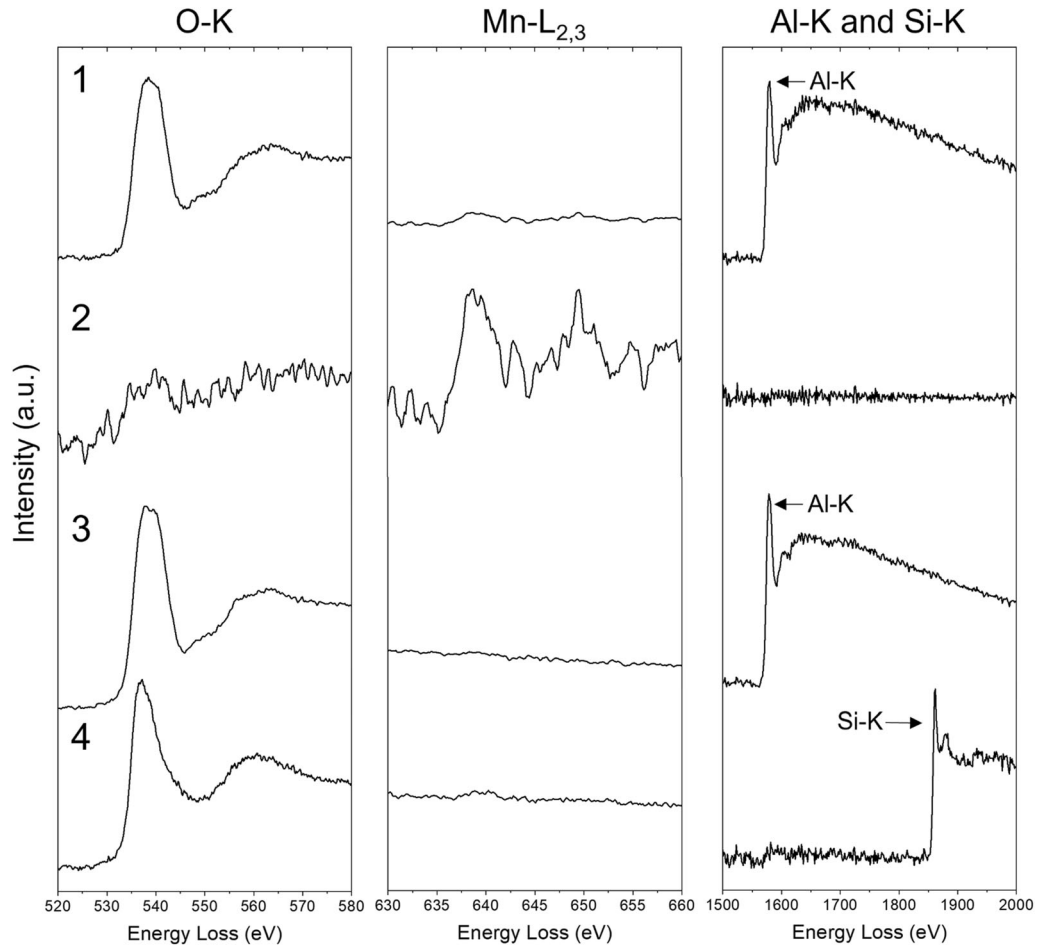


Fig. 19—EELS spectra showing the O-K, Mn-L_{2,3}, Al-K, and Si-K edges from the numbered regions in Fig. 18 taken from the MF – 10 °C dp sample.

Table V. Calculated Solubility Products for Oxide Species of Interest in Fe at 1163 K

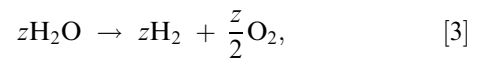
Oxide Species	Al ₂ O ₃	MnAl ₂ O ₄	MnO	Mn ₂ SiO ₄	SiO ₂
Solubility Product	8.08×10^{-15} (ppm) ⁵	5.82×10^{-15} (ppm) ⁷	43.46 (ppm) ²	1.84×10^{-2} (ppm) ⁷	1.19×10^{-3} (ppm) ³

In this and subsequent equations, the terms pertaining to N can be removed in the case of a binary oxide M_xO_z . At equilibrium, the standard Gibbs free energy of Eq. [1] is expressed by

$$\Delta G_1^{\circ} = -RT \ln K_1 = -RT \ln \left(\frac{(pH_2)^z}{a_M^x a_N^y (pH_2O)^z} \right), \quad [2]$$

where R is the universal gas constant, T is the absolute temperature, pH_2 is the partial pressure of hydrogen (0.05 in the present case), pH_2O is the partial pressure of water vapor, and a_i is the activity of a general

solute species (where it is assumed that oxides are pure condensed species and, therefore, have unit activity). For a given process atmosphere dew point with a fixed pH_2 , it should be noted that the $\frac{pH_2}{pH_2O}$ ratio is constant. Equation 1 can be written as the sum of Eq. [3], the decomposition of water vapor, and Eq. [4], the formation of the general ternary oxide from its constituent species:



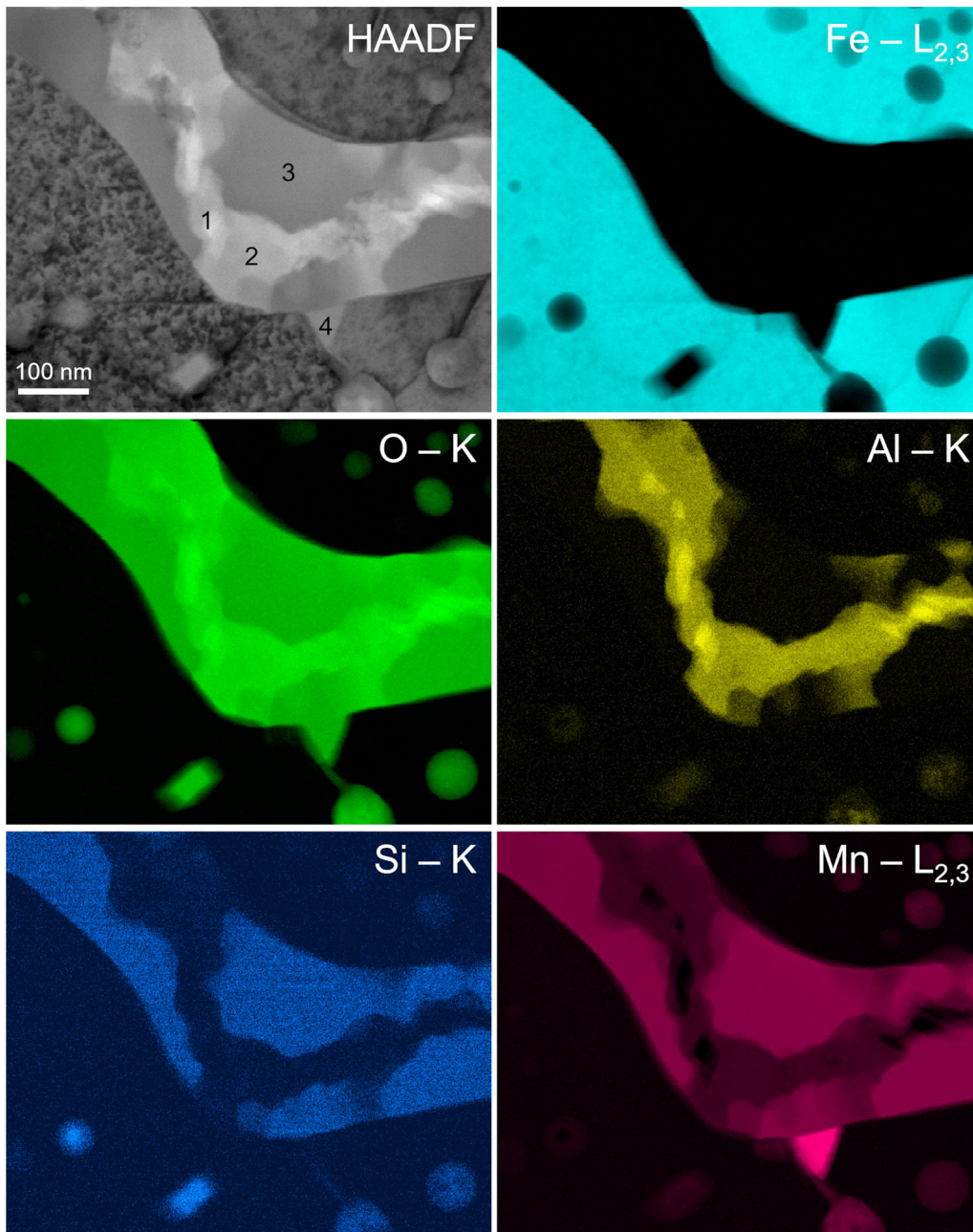
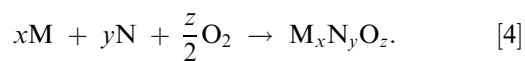


Fig. 20—HAADF image and EELS elemental maps of Fe, O, Al, Si, and Mn showing a representative selective grain boundary oxide structure in the IA - 10 °C/- 10 °C dp sample.



The oxygen potential (*i.e.*, oxygen partial pressure, pO_2) for the formation of a selective oxide species as a function of temperature is plotted along with the process atmosphere pO_2 for dew points of -30 °C, -10 °C, and + 5 °C in Figure 22(a). A detailed view of this plot, emphasizing the austenitization temperature of 1163 K,

is shown in Figure 22(b). From Figure 22, it is apparent that the thermodynamic driving force for the formation of Al_2O_3 is the greatest, as documented by the annotated ΔG_1^0 in Figure 22(b) from Eq. [2], followed by $MnAl_2O_4$, SiO_2 , $MnSiO_3/Mn_2SiO_4$, and MnO in order of decreasing thermodynamic driving force for formation.

Although oxide structures with layers corresponding approximately to the thermodynamic stability of the constituent oxides were observed, the kinetic factors for

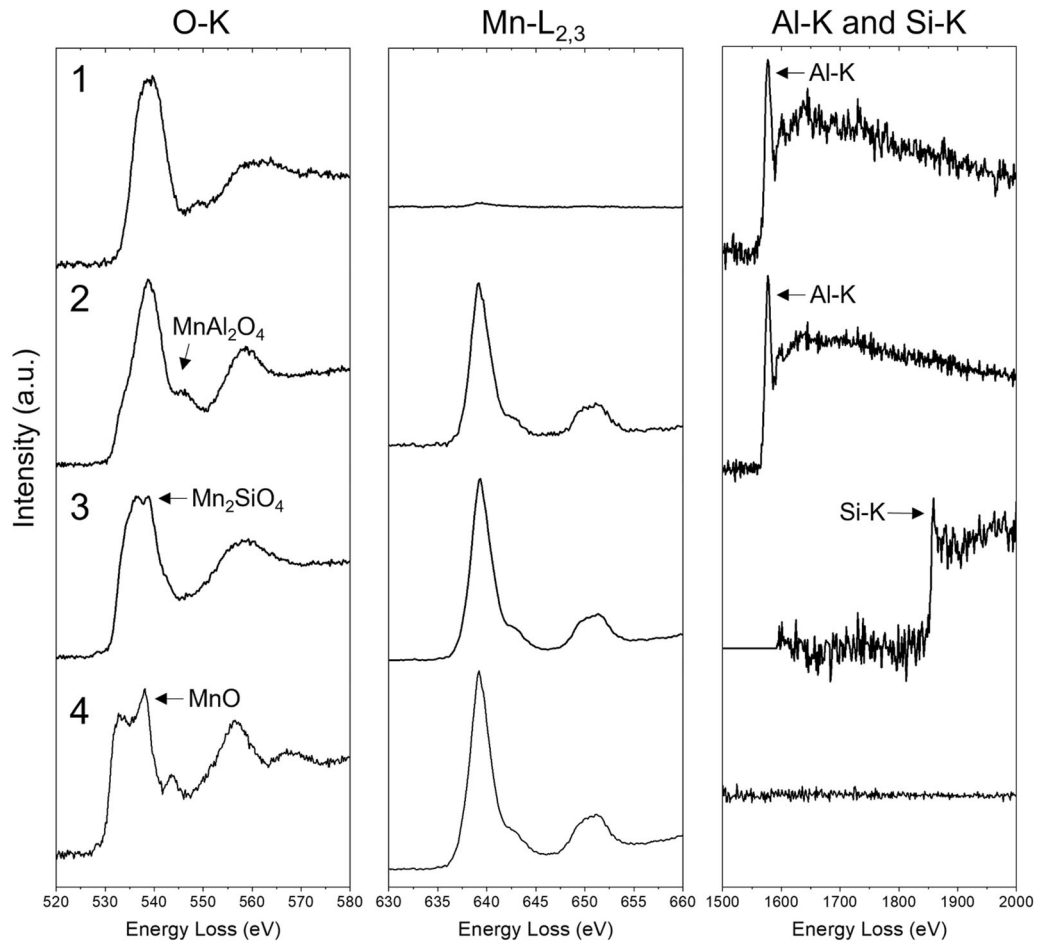


Fig. 21—EELS spectra showing the O-K, Mn-L_{2,3}, Al-K, and Si-K edges from the numbered regions in Fig. 20 (IA – 10 °C/– 10 °C dp sample).

oxide formation also influenced the final morphology of the internal and external oxides. The spatial distribution and morphology of the external oxides are of particular interest due to the known consequences of external oxides on the reactive wetting of steel substrates by Zn(Al,Fe) galvanizing baths. Given that the flash pickling treatment did not remove the MnAl₂O₄, the co-precipitation of MnAl₂O₄ and MnSiO₃/Mn₂SiO₄ (such that neither species formed a continuous layer, see Figure 11) beneath the MnO nodules is a favorable outcome that provided bold exposure of significant area fractions of metallic Fe on the substrate surface to the Zn(Al,Fe) bath.

A comparison of the pickled (Figures 4 and 13) and intercritically annealed samples (Figures 5 and 15) reveals that the morphology and chemical composition of the external oxide nodules did not change significantly during intercritical annealing. This is corroborated by the box plot in Figure 7 showing similar

external oxide thickness distributions for the pickled and intercritically annealed samples, as well as the XPS profiles in Figure 10 showing similar elemental depth profiles for the P – 10 °C dp and the intercritically annealed samples. This is attributed to the depletion of alloying elements in the near-surface bulk material, as shown by the lack of Al, Mn, and Si signals in EELS spectra for Region 5 in the MF – 10 °C dp sample (Figures 11 and 12) and Region 1 in the P – 10 °C dp sample (Figures 13 and 14). This implies that the intercritical annealing cycle was insufficiently long and at an insufficiently high temperature to allow for diffusion of ignoble solute elements from deeper in the substrate to the surface, thus, maintaining the existent pickled surface microstructure. This finding is in agreement with the work published by Bhadhon and McDermid in their study on a 0.2C-5.9Mn-1.5Si-0.4Al-0.6Cr prototype 3G AHSS which underwent a similar thermal cycle.^[72]

Table VI. Summary of the External and Internal Oxide Evolution for the MF – 10 °C dp Sample After Each Processing Step, as Determined by TEM–EELS

	MF – 10 °C dp	P –10 °C dp	IA –10 °C/–30 °C dp IA –10 °C/–10 °C dp IA –10 °C/ + 5 °C dp
External Oxides	100–200 nm nodular oxides, extensive surface coverage, MnO (outer layer) → MnSiO ₃ /Mn ₂ SiO ₄ /MnAl ₂ O ₄ (inner layer)	only discrete MnAl ₂ O ₄ nodules remain (~ 50 nm)	no significant change
Internal Oxides (< 2 μm deep)	bulk and grain boundary MnSiO ₃ /Mn ₂ SiO ₄ oxides with veins of MnAl ₂ O ₄ /Al ₂ O ₃	selective dissolution of MnSiO ₃ /Mn ₂ SiO ₄ in near-surface grain boundary structures	no significant change
Internal Oxides (2–8 μm deep)	grain boundary oxides with MnAl ₂ O ₄ /Al ₂ O ₃ cores and MnSiO ₃ /Mn ₂ SiO ₄ shells	no significant change	no significant change
Internal Oxides (8–12 μm deep)	grain boundary oxides with separate layers of SiO ₂ and Al ₂ O ₃ , scant MnO	no significant change	no significant change

These results can be modeled approximately using the solution to Fick’s second law of diffusion for the case of diffusion between two semi-infinite solids with different initial solute concentrations. In this case, it is assumed that the solute-depleted near-surface layer is coupled with a substrate with the bulk concentration reported in Table I (*i.e.*, 5.45 at. pct Mn, 3.77 at. pct Al, and 2.11 at. pct Si). The solution to Fick’s second law for this configuration is provided in Eq. [5]:

$$C(y, t) = C_1 + \frac{C_2 - C_1}{2} \left[1 + \operatorname{erf} \left(\frac{y}{2\sqrt{Dt}} \right) \right] \quad [5]$$

where $C(y, t)$ is the concentration of solute at position y (where $y = 0$ represents the position of the initial interface) at time t ; C_1 is the bulk concentration of a given solute (in mole fraction, Table I); C_2 is the concentration of a given solute in the near-surface solute-depleted layer and D is the diffusivity of solute in the matrix at 983 K (calculated from the data presented in Table VII). The initial (*i.e.*, $t = 0$ s) boundary conditions for the system are provided in Eqs. [6] and [7], where the case of a solute-free near-surface layer (*i.e.*, $C_2 = 0.000$) represents the most severe approach to modeling solute diffusion.

$$C(y, t) = C_1 = \text{bulk concentration of solute for } y < 0 \quad [6]$$

(see Table I)

$$C(y, 0) = C_2 = 0.000 \text{ for } y \geq 0. \quad [7]$$

The resulting concentration profiles for Mn, Al, and Si diffusion are presented in Figure 23 and show that 120 s at 983 K is insufficient to transport solutes to the surface, even when modeling the most extreme initial solute concentration gradient. In the most pessimistic scenario (*i.e.*, in ferrite), only 500 nm of the solute-depleted near-surface layer is re-enriched during intercritical annealing whereas the internal oxide network (and, therefore, the solute-depleted matrix) is several microns deep (as shown in Figure 8) and the EELS maps and spectra in Region 4 of Figures 16 and 17 show solute depletion to approximately 3 μm in depth. Thus, no significant Al, Si, or Mn would be expected to diffuse to the surface during intercritical annealing to oxidize and modify the surface structures from the antecedent MnAl₂O₄ nodules observed after flash pickling. This corroborates the findings in Figures 5, 7, 10, and 15 showing that the external oxide structures did not change significantly during the IA treatment.

The internal oxide network that formed during the MF annealing step also did not change significantly during intercritical annealing. Furthermore, the MF and corresponding IA samples had similar internal oxide depths (as shown in Figure 8) and structures (comparing Figure 16 (MF – 10 °C dp) and Figure 20 (IA – 10 °C/– 10 °C dp) and summarized in Table VI). The core-shell oxide structures formed during MF annealing comprised an Al₂O₃ or

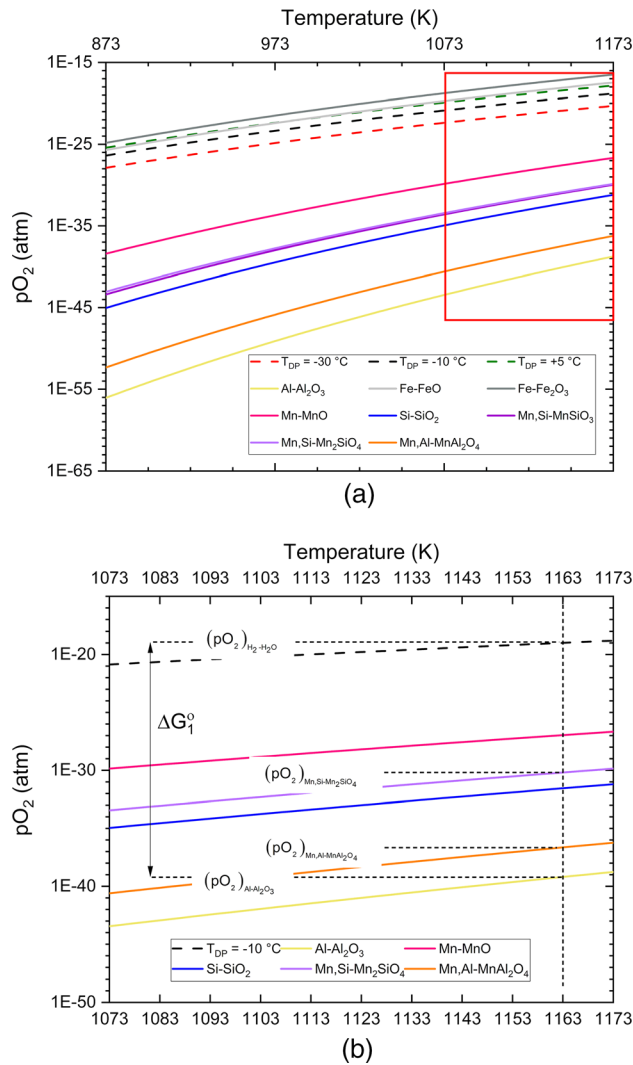


Fig. 22—(a) Critical oxygen partial pressures for the oxidation of relevant metallic elements in a N_2 -5 pct H_2 atmosphere as a function of annealing temperature, assuming unit activity of the metallic species. The oxygen partial pressures for a $-30^\circ C$, $-10^\circ C$, and $+5^\circ C$ dew point process atmosphere are also included. (b) Detailed view of (a) highlighting the austenitization temperature of 1163 K and $-10^\circ C$ process atmosphere. Data obtained from FREED^[47] and Jung *et al.*^[71].

$MnAl_2O_4$ core surrounded with a Mn_2SiO_4 shell. Intercritical annealing may have allowed for some MnO nodule precipitation on the shell (Figure 20) and MnO reaction with core Al_2O_3 to form additional $MnAl_2O_4$. The deepest part of the oxide network in both MF and IA samples comprised Al_2O_3 and SiO_2 (such as the oxide shown in Figure 18), suggesting that these highly insoluble (Table V) and

thermodynamically stable oxide species (Figure 22) formed initially and provided a scaffold for MnO nucleation and complex oxidation.

A summative schematic of the oxide and surface microstructural structure evolution is shown in Figure 24:

(a) The initial oxide-free microstructure.

(b) The near-surface region is dealloyed due to the formation of internal bulk and grain boundary oxides and external oxides. Pure Fe nodules are also formed as a result of the volumetric expansion associated with internal oxidation.

(c) The pickling solution dissolves most of the external oxides, revealing a significant surface area fraction of near-pure Fe. Some internal oxides with connection to the surface are also dissolved by the pickling solution.

(d) The intercritical annealing step results in some restoration of solute by diffusion from the deeper bulk microstructure to the bottom of the dealloyed layer, but the surface structures remain unchanged from (c).

It is noteworthy that Figure 24(d) depicts a surface that shows the potential to form high-quality and formable galvanized coatings due to the significant area fractions of boldly exposed Fe and Fe nodules with limited coverage by small, discrete, dispersed oxides.

The results of this study show that promising results for future reactive wetting studies have been obtained when austenitizing at a dew point of $-30^\circ C$, $-10^\circ C$, or $+5^\circ C$. However, it is noteworthy that the general microstructure and chemistry of the external oxides arising from this thermal treatment are not significantly different (see Figures 3, 7, 11, 12 and Table VI). This result likely arises from the high-temperature/long-duration nature of this annealing treatment being only a weak function of both time and process atmosphere pO_2 —*i.e.*, near the plateau in the parabolic rate curves common to these alloys.^[16,32,37] Thus, it is not possible to define generalized practical limits for the process atmosphere dew point during austenitization of the present medium-Mn 3G AHSS and short-duration austenitization times may change the oxide thickness as a function of process atmosphere dew point (*i.e.*, pO_2). Future research efforts should focus on minimizing the austenitization time such that global mechanical properties are maintained while documenting its effect on both external and internal oxidation kinetics and microstructural development. Future research should also focus on determining the effects of internal oxidation depth on other important properties (such as fatigue, bending angle, weldability, *etc.*) within the context of optimizing the austenitization process atmosphere dew point.

Table VII. Diffusion Data for Al, Mn, and Si in Ferrite and Austenite Used to Calculate Their Approximate Diffusion Distances after 120 s at 983 K

Phase	Element/Compound	$D'_i (\times 10^4 \text{ m}^2/\text{s})$	$Q_i (\times 10^3 \text{ J/mol})$	References
Ferrite	Mn	0.756	224	73
	Al	5.15	246	74
	Si	0.927	220	75
Austenite	Mn	0.178	264	73
	Al	5.9	242	76
	Si	0.21	242	77

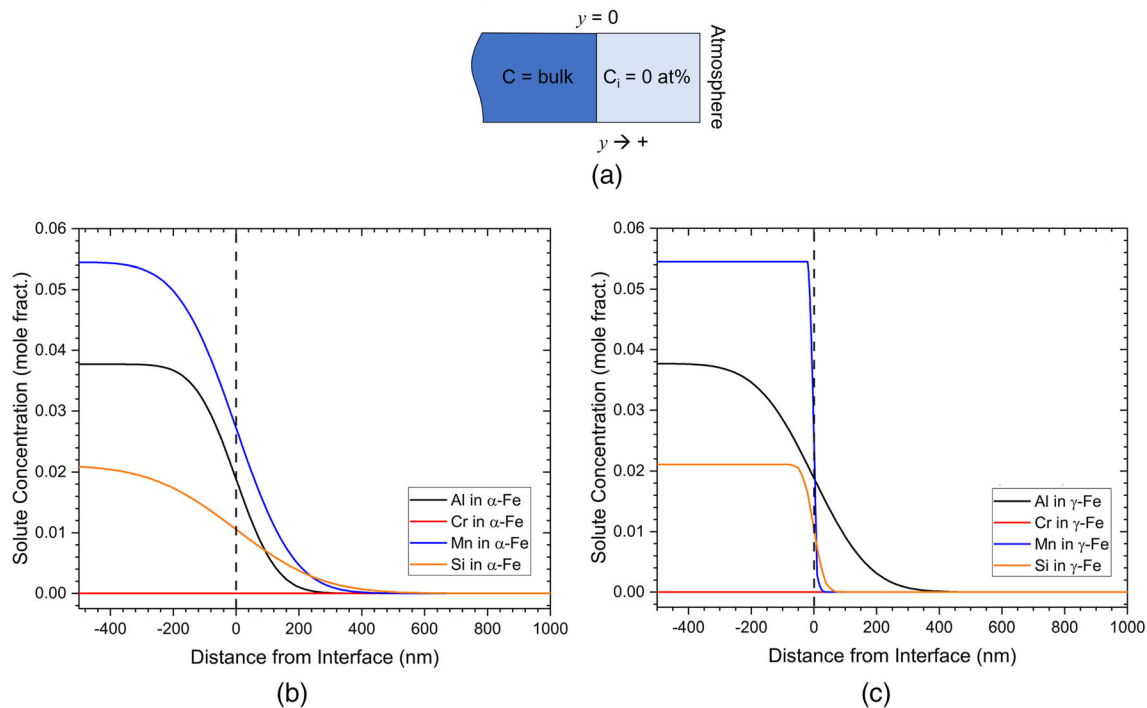


Fig. 23—(a) Schematic of the diffusion couple proposed to model the diffusion of the solute from the substrate bulk to the pre-oxidized near-surface layer; calculated concentrations of Mn, Al, and Si as a function of distance from the interface after 120 s at 983 K for solutes diffusing in (b) ferrite and (c) austenite.

V. CONCLUSIONS

The selective oxidation of a 0.15C-5.6Mn-1.9Al-1.1Si (wt pct) prototype steel during two-stage annealing with intermediate flash pickling was documented using SEM + FIB, XPS, and TEM-EELS. It was concluded that

1. Austenitizing at 1163 K for 600 s (to obtain a martensitic-ferritic microstructure) at process atmosphere dew points of -30°C , -10°C , or $+5^\circ\text{C}$ resulted in the formation of a 200-nm thick, compact external oxide layer for the three dew points used in this work. It was found that compact nodules of MnO formed on top of co-precipitated

nodules of $\text{MnSiO}_3/\text{Mn}_2\text{SiO}_4$ and MnAl_2O_4 . It was further determined that the depth of internal oxidation increased with increasing process atmosphere dew point.

2. The intermediate flash pickling treatment effectively dissolved the external MnO, MnSiO_3 , and Mn_2SiO_4 , along with some near-surface internal oxide structures. It was observed that MnAl_2O_4 was the only major external oxide species present after flash pickling, likely due to its low solubility in hydrochloric acid solutions.
3. No significant changes to external oxide thickness, surface density, or chemical speciation were observed after intercritical annealing. During the

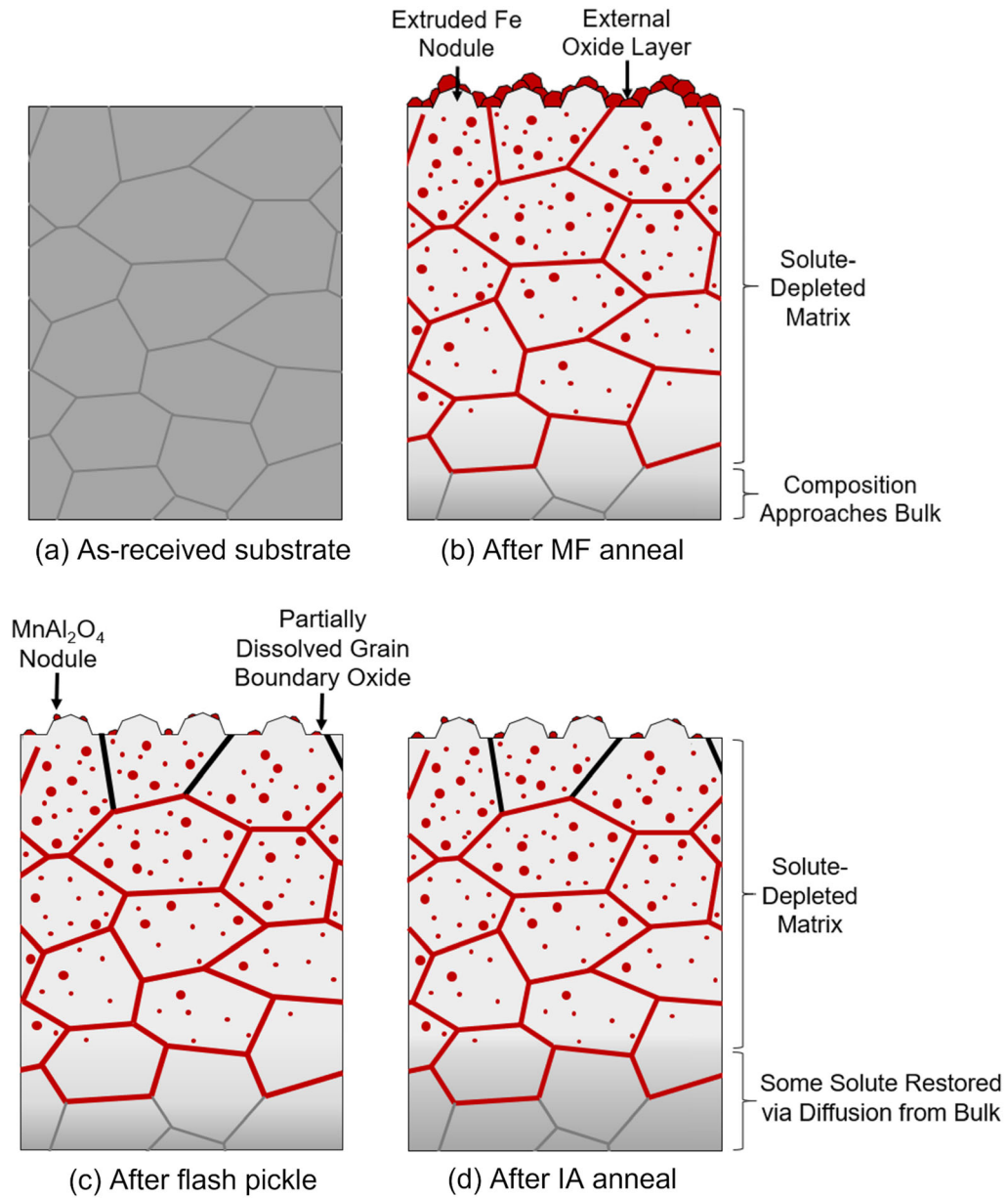


Fig. 24—Summative schematic of the evolution of the surface and sub-surface structures (a) in the as-received condition; (b) after austenitization; (c) after flash pickling; (d) after intercritical annealing.

MF treatment, the near-surface matrix was depleted in solute due to the oxidation of Mn, Si, and Al. As such, the subsequent IA time and temperature were insufficient for diffusion of these species from the bulk matrix to the surface to result in further external oxidation.

4. The final surfaces documented in this investigation show promise for future galvanizing trials due to the wide spacing of nano-scaled oxide nodules with significant area fractions of metallic Fe directly exposed to the galvanizing bath, thus, facilitating reactive wetting.

ACKNOWLEDGMENTS

Financial support for this research was provided by the Natural Sciences and Engineering Research Council of Canada (NSERC) Grant CRDPJ 522309-17 (with partners ArcelorMittal Dofasco Inc., The Electromac Group, HudBay Minerals Inc., Stelco Inc., Teck Metals Limited, and the International Zinc Association Galvanized Autobody Partnership (IZA--GAP)). United States Steel Research (Munhall) is acknowledged for their generous provision of the experimental substrate used in this project. Technical assistance provided by members of the McMaster Steel

Research Centre; the Centre for Automotive Materials and Corrosion; the Biointerfaces Institute, the Brockhouse Institute for Materials Research; and the Canadian Centre for Electron Microscopy is appreciated.

CONFLICT OF INTEREST

On behalf of all authors, the corresponding author states that there is no conflict of interest.

REFERENCES

1. D.K. Matlock and J.G. Speer: in *Proceedings of the 3rd International Conference on Structural Steels*, H.C. Lee, ed., Korean Institute of Metals and Materials, Seoul, Korea, 2006, pp. 774–81.
2. D.K. Matlock and J.G. Speer: *Third Generation of AHSS: Microstructure Design Concepts*, Springer, Jamshedpur, 2009.
3. E. De Moor, P.J. Gibbs, J.G. Speer, and D.K. Matlock: *AIST Trans.*, 2010, vol. 7, pp. 133–44.
4. D.K. Matlock, J.G. Speer, E. De Moor, and P.J. Gibbs: *JES-TECH*, 2012, vol. 15, pp. 1–2.
5. K.M.H. Bhadhon, J.R. McDermid, and F.E. Goodwin: in *Proc. 10th Conf. on Zinc and Zinc Alloy Coated Steel Sheet, Galvatech 2015*, Toronto, 2015, pp. 936–43.
6. K.M.H. Bhadhon, J.R. McDermid, X. Wang, E.A. McNally, and F.E. Goodwin: in *Proc. 11th Conf. on Zinc and Zinc Alloy Coated Steel Sheet, Galvatech 2017*, ISIJ International, Tokyo, 2017, pp. 493–500.
7. D.M. Pallisco, J.R. McDermid, E.A. McNally, and F.E. Goodwin: in *Proc. 11th Conf. on Zinc and Zinc Alloy Coated Steel Sheet, Galvatech 2017*, Tokyo, 2017, pp. 782–89.
8. D.M. Pallisco, K.M.H. Bhadhon, V. Patel, M. Pourmajidian, F.E. Goodwin, and J.R. McDermid: in *Proc. 4th Int'l Conf. on Medium and High-Manganese Steels*, 2019, pp. 375–78.
9. V. Patel: McMaster University, 2019.
10. D.M. Pallisco and J.R. McDermid: *Mater. Sci. Eng. A*, 2020, vol. 778, 139111.
11. J. Mahieu, S. Claessens, B.C. De Cooman, and F.E. Goodwin: in *Galvatech 2004 Proceedings*, M.A. Baker, ed., Association for Iron and Steel Technology, Chicago, IL, 2004, pp. 529–38.
12. E.M. Bellhouse and J.R. McDermid: *Metall. Mater. Trans. A*, 2011, vol. 42A, pp. 2753–68.
13. E.M. Bellhouse and J.R. McDermid: *Metall. Mater. Trans. A*, 2012, vol. 43, pp. 2426–41.
14. R. Sagl, A. Jarosik, D. Stifter, and G. Angeli: *Corros. Sci.*, 2013, vol. 70, pp. 268–75.
15. R. Sagl, A. Jarosik, G. Angeli, T. Haunschmied, G. Hesser, and D. Stifter: *Acta Mater.*, 2014, vol. 72, pp. 192–99.
16. M. Pourmajidian and J.R. McDermid: *Metall. Mater. Trans. A*, 2018, vol. 49A, pp. 1795–1808.
17. G. Seyed Mousavi and J.R. McDermid: *Metall. Mater. Trans. A*, 2018, vol. 49A, pp. 5546–60.
18. J. Mahieu, S. Claessens, and B.C. De Cooman: *Metall. Mater. Trans. A*, 2001, vol. 32A, pp. 2905–2908.
19. P. Drillet, Z. Zermout, D. Bouleau, J. Maigne, and S. Claessens: in *Galvatech 2004 Proceedings*, M.A. Baker, ed., Association for Iron and Steel Technology, Chicago, IL, 2004, pp. 1123–34.
20. E.M. Bellhouse and J.R. McDermid: *Metall. Mater. Trans. A*, 2010, vol. 41A, pp. 1539–53.
21. S. Alibeigi, R. Kavitha, R.J. Meguerian, and J.R. McDermid: *Acta Mater.*, 2011, vol. 59, pp. 3537–49.
22. S. Prabhudev, S. Swaminathan, and M. Rohwerder: *Corros. Sci.*, 2011, vol. 53, pp. 2413–18.
23. M. Norden, M. Blumenau, T. Wuttke, and K.J. Peters: *Appl. Surf. Sci.*, 2013, vol. 271, pp. 19–31.
24. E.M. Bellhouse and J.R. McDermid: *Mater. Sci. Eng. A*, 2008, vol. 491, pp. 39–46.
25. Y. Tobiya and C. Kato: *Tetsu-to-Hagané*, 2003, vol. 89, pp. 38–45.
26. R. Khondker, A.I.M. Mertens, and J.R. McDermid: *Mater. Sci. Eng. A*, 2007, vol. 463, pp. 157–65.
27. E.M. Bellhouse and J.R. McDermid: *Metall. Mater. Trans. A*, 2010, vol. 41A, pp. 1460–73.
28. R. Kavitha and J.R. McDermid: *Surf. Coat. Technol.*, 2012, vol. 212, pp. 152–58.
29. L. Cho, J.S. Lee, M.S. Kim, Y.H. Kim, and B.C. De Cooman: *Metall. Mater. Trans. A*, 2013, vol. 44A, pp. 362–71.
30. L. Cho, M.S. Kim, Y.H. Kim, and B.C. De Cooman: *Metall. Mater. Trans. A*, 2013, vol. 44A, pp. 5081–95.
31. Y. Suzuki, T. Yamashita, Y. Sugimoto, S. Fujita, and S. Yamaguchi: *ISIJ Int.*, 2009, vol. 49, pp. 564–73.
32. O. Matsumura, Y. Sakuma, and H. Takechi: *Trans. ISIJ*, 1987, vol. 27, pp. 570–79.
33. J. Maki, J. Mahieu, B.C. De Cooman, and S. Claessens: *Mater. Sci. Technol.*, 2003, vol. 19, pp. 125–31.
34. M. Pourmajidian and J.R. McDermid: *ISIJ Int.*, 2018, vol. 58, pp. 1635–43.
35. L. Cho, M.S. Kim, Y.H. Kim, and B.C. De Cooman: *Metall. Mater. Trans. A*, 2014, vol. 45A, pp. 4484–98.
36. L. Cho, E.J. Seo, G.S. Jung, D.W. Suh, and B.C. De Cooman: *Metall. Mater. Trans. A*, 2016, vol. 47A, pp. 1705–19.
37. M. Pourmajidian, B. Langelier, and J.R. McDermid: *Metall. Mater. Trans. A*, 2018, vol. 49A, pp. 5561–73.
38. G. Seyed Mousavi, B. Langelier, and J.R. McDermid: *Metall. Mater. Trans. A*, 2019, vol. 50A, pp. 2898–11.
39. M. Pourmajidian and J.R. McDermid: *Surf. Coat. Technol.*, 2019, vol. 357, pp. 418–26.
40. J. Oh, L. Cho, M.S. Kim, K. Kang, and B.C. De Cooman: *Metall. Mater. Trans. A*, 2016, vol. 47A, pp. 5474–86.
41. Y.F. Gong, H.S. Kim, and B.C. De Cooman: *ISIJ Int.*, 2009, vol. 49, pp. 557–63.
42. L. Cho, G.S. Jung, and B.C. De Cooman: *Metall. Mater. Trans. A*, 2014, vol. 45A, pp. 5158–72.
43. G. Seyed Mousavi and J.R. McDermid: *Surf. Coat. Technol.*, 2018, vol. 351, pp. 11–20.
44. H. Luo and H. Dong: *Mater. Sci. Eng. A*, 2015, vol. 626, pp. 207–12.
45. K.M.H. Bhadhon: McMaster University, 2017.
46. K. Steineder, D. Krizan, R. Schneider, C. Béal, and C. Sommitsch: *Acta Mater.*, 2017, vol. 139, pp. 39–50.
47. A.E. Morris: 2013.
48. M. Oku and K. Hirokawa: *J. Electron. Spectros. Relat. Phenomena*, 1976, vol. 8, pp. 475–81.
49. S.L.T. Andersson and M.S. Scurrell: *J. Catal.*, 1979, vol. 59, pp. 340–56.
50. B.R. Strohmeier and D.M. Hercules: *J. Phys. Chem.*, 1984, vol. 88, pp. 4922–29.
51. J. Finster: 1988, vol. 12, pp. 309–14.
52. J.F. Moulder, W.F. Stickle, P.E. Sobol, and K.D. Bomben: *Handbook of X-Ray Photoelectron Spectroscopy*, Physical Electronics Inc, Eden Prairie, MN, 1995.
53. A.P. Grosvenor, E.M. Bellhouse, A. Korinek, M. Bugnet, and J.R. McDermid: *J. Appl. Surf. Sci.*, 2016, vol. 379, pp. 242–48.
54. J.H. Rask, B.A. Miner, and P.R. Buseck: *Ultramicroscopy*, 1987, vol. 21, pp. 321–26.
55. M. Sternitzke and G. Müller: *J. Am. Ceram. Soc.*, 1994, vol. 77, pp. 737–42.
56. K. Naoe, M. Nishiki, and K. Sato: *J. Therm. Spray Technol.*, 2014, vol. 23, pp. 1333–38.
57. C.F. Jones, R.S.C. Smart, and P.S. Turner: *J. Chem. Soc. Faraday Trans.*, 1990, vol. 86, pp. 947–53.
58. J.F. Banfield, G.G. Ferruzzi, W.H. Casey, and H.R. Westrich: *Geochemica Cosm. Acta*, 1995, vol. 59, pp. 19–31.
59. W.H. Casey, M.F. Hochella, and H.R. Westrich: *Geochim. Cosmochim. Acta*, 1993, vol. 57, pp. 785–93.
60. C.R. Shastry, J.A. Rotole, and T.W. Kaiser: *7th Int. Conf. Zinc Zinc Alloy Coat. Steel Sheet*, 2007, p. Paper B-6-2, 403–408.
61. X.S. Li, S.-I. Baek, C.-S. Oh, S.-J. Kim, and Y.-W. Kim: *Ser. Mater.*, 2007, vol. 57, pp. 113–16.
62. Y.F. Gong, H.S. Kim, and B.C. De Cooman: *ISIJ Int.*, 2008, vol. 48, pp. 1745–51.
63. Y.F. Gong, Y.R. Lee, H.S. Kim, and B.C. De Cooman: in *Asia-Pacific Galvanizing Conference 2009 Proceedings*, Jeju Island, South Korea, 2009, p. paper A-41.

64. G. Seyed Mousavi and J.R. McDermid: in *Proc. 11th Conf. on Zinc and Zinc Alloy Coated Steel Sheet, Galvatech 2017*, 2017, pp. 485–92.
65. X.S. Li, S.-I. Baek, C.-S. Oh, S.-J. Kim, and Y.-W. Kim: *Scr. Mater.*, 2008, vol. 59, pp. 290–93.
66. C.C. Ahn, O.L. Krivanek, Gatan Inc., and Arizona State University: *EELS Atlas: A Reference Collection of Electron Energy Loss Spectra Covering All Stable Elements*, Gatan, Inc., Warrendale, PA, USA, 1983.
67. G. Kissinger, M.A. Schubert, D. Kot, and T. Grabolla: *ECS J. Solid State Sci. Technol.*, 2017, vol. 6, pp. N54-63.
68. G. Eriksson, P. Wu, M. Blander, and A.D. Pelton: *Can. Metall. Q.*, 1994, vol. 13, pp. 13–21.
69. Thermodata: 2005.
70. D. Huin, P. Flauder, and J.-B. Leblond: *Oxid. Met.*, 2005, vol. 64, pp. 131–67.
71. I.H. Jung, Y.B. Kang, S.A. Decterov, and A.D. Pelton: *Metall. Mater. Trans. B Process Metall. Mater. Process. Sci.*, 2004, vol. 35, pp. 259–68.
72. K.M.H. Bhadhon and J.R. McDermid: *J. Electrochem. Soc.*, 2022, vol. 169, 061504.
73. H. Oikawa: *Technology Reports*, 1983.
74. J. Takada, S. Yamamoto, S. Kikuchi, and M. Adachi: *Oxid. Met.*, 1986, vol. 25, pp. 93–105.
75. R.J. Borg and D.Y.F. Lai: *J. Appl. Phys.*, 1970, vol. 41, pp. 5193–200.
76. Diffusion Information Center: *Diffusion Data: A Continuous Compilation of New Reference Data on Diffusion Processes in Inorganic Solids and Their Melts*, 1969.
77. J. Takada, K. Kashiwagi, and M. Adachi: *J. Mater. Sci.*, 1984, 19, vol. 19.

Publisher's Note Springer Nature remains neutral with regard to jurisdictional claims in published maps and institutional affiliations.

Springer Nature or its licensor (e.g. a society or other partner) holds exclusive rights to this article under a publishing agreement with the author(s) or other rightsholder(s); author self-archiving of the accepted manuscript version of this article is solely governed by the terms of such publishing agreement and applicable law.